

Air Force Institute of Technology

AFIT Scholar

Theses and Dissertations

Student Graduate Works

3-2021

Amplitude Estimation for the Large Clutter Discrete Removal Algorithm

Hannah Gjermo Chomitz

Follow this and additional works at: <https://scholar.afit.edu/etd>



Part of the [Theory and Algorithms Commons](#)

Recommended Citation

Gjermo Chomitz, Hannah, "Amplitude Estimation for the Large Clutter Discrete Removal Algorithm" (2021). *Theses and Dissertations*. 4985.

<https://scholar.afit.edu/etd/4985>

This Thesis is brought to you for free and open access by the Student Graduate Works at AFIT Scholar. It has been accepted for inclusion in Theses and Dissertations by an authorized administrator of AFIT Scholar. For more information, please contact AFIT.ENWL.Repository@us.af.mil.



**AMPLITUDE ESTIMATION FOR THE
LARGE CLUTTER DISCRETE REMOVAL ALGORITHM**

THESIS

Hanna Gjermo Chomitz, 1st Lt, USAF

AFIT-MS-ENG-21-M-40

**DEPARTMENT OF THE AIR FORCE
AIR UNIVERSITY**

AIR FORCE INSTITUTE OF TECHNOLOGY

Wright-Patterson Air Force Base, Ohio

DISTRIBUTION STATEMENT A:
APPROVED FOR PUBLIC RELEASE; DISTRIBUTION UNLIMITED

The views expressed in this thesis are those of the author and do not reflect the official policy or position of the United States Air Force, the Department of Defense, or the United States Government.

This material is declared a work of the U.S. Government and is not subject to copyright protection in the United States.

AFIT-MS-ENG-21-M-40

AMPLITUDE ESTIMATION FOR THE
LARGE CLUTTER DISCRETE REMOVAL ALGORITHM

THESIS

Presented to the Faculty
Department of Electrical and Computer Engineering
Graduate School of Engineering and Management
Air Force Institute of Technology
Air University
Air Education and Training Command
in Partial Fulfillment of the Requirements for the
Degree of Master of Science in Electrical Engineering

Hanna Gjerme Chomitz, B.S.

1st Lt, USAF

March 2021

DISTRIBUTION STATEMENT A:
APPROVED FOR PUBLIC RELEASE; DISTRIBUTION UNLIMITED

AFIT-MS-ENG-21-M-40

AMPLITUDE ESTIMATION FOR THE
LARGE CLUTTER DISCRETE REMOVAL ALGORITHM

Hanna Gjermo Chomitz, B.S.

1st Lt, USAF

Committee Membership:

Maj James R. Lievsay, PhD
Chair

Julie Ann Jackson, PhD
Member

Richard Martin, PhD
Member

Abstract

A large clutter discrete (LCD) is spectrally bright localized clutter that can cause a false alarm or missed target detection in space-time adaptive processing (STAP) radar data. For passive bistatic STAP, the four step LCD removal (LCDR) algorithm estimates the spatial/Doppler frequency and complex amplitude of the LCD and then removes it from the data. Once the LCD is removed from the data, homogeneous clutter suppression techniques can be used to process the data and search for targets. This research focuses on reducing the complexity of estimating the LCD's complex amplitude. This research proposes a method that directly solves for the amplitude that minimizes the power output at the LCD's spatial/Doppler frequency. This research also focuses on further verifying the LCDR algorithm through hardware experimentation. Previously, the algorithm has only been tested through simulation.

First, the amplitude estimation technique is tested through MATLAB simulations to determine the efficiency and accuracy of the proposed method. Then, a hardware experiment is used to test the amplitude estimation technique and verify the LCDR algorithm in a laboratory environment.

The MATLAB simulations prove the proposed amplitude estimation technique is faster than the original method published in [11]. The LCDR algorithm is able to successfully remove the LCD in the simulated data so the clutter can be treated as homogeneous. The hardware results are less conclusive. The hardware adds additional complications to the data because of grating lobes and the limited number of channels available. However, the LCDR algorithm is able to remove portions of the LCD and shows promise of being successful in more real world environments.

Acknowledgments

First, I would like to thank my husband for his love and support. Additionally, I would like to thank my parents and sisters for their continued guidance and encouragement throughout my education.

I would like thank my advisor, Lt Col(s) J.R. Lievsay, for sharing his expertise on radar systems and providing guidance on my research. I appreciate his professional mentorship on life, academics, and my military career.

I would like to thank the AFRL Sensors Directorate for lending me their phased array, which was a crucial component to my research. I would also like to extend my gratitude to Mr. Michael Hill and Ms. Angela Hayden for their technical support. Their efforts were critical to the successful completion of my laboratory experiments.

Additionally, I would like to thank my thesis committee members, Dr. Julie Ann Jackson and Dr. Richard Martin, for their time and advice.

Hanna Gjermo Chomitz

Table of Contents

	Page
Abstract	iv
Acknowledgments	v
Table of Contents	vi
List of Figures	viii
List of Tables	x
List of Symbols	xi
List of Acronyms	xiv
I. Introduction	1
1.1 Introduction	1
1.2 Problem Statement	3
1.3 Scope	3
1.4 Structure	3
II. Background	5
2.1 Introduction	5
2.2 Radar	6
2.2.1 Linear Frequency Modulation (LFM) Pulse Signal Model	7
2.3 Space-Time Adaptive Processing (STAP)	12
2.3.1 Monostatic STAP Model	12
2.3.2 Passive Bistatic Radar (PBR)	16
2.3.3 Passive STAP Clutter Model	18
2.3.4 Clutter Ridge	21
2.4 Long-Term Evolution (LTE) Waveforms	21
2.5 Previous Research on Clutter Suppression and LCD Removal	23
2.5.1 Homogeneous Clutter Suppression	23
2.5.2 LCD Removal	23
2.6 LCDR Algorithm	24
2.6.1 Step One	25
2.6.2 Step Two	25

	Page
2.6.3 Step Three	27
2.6.4 Step Four	28
2.7 Output Power at a Spatial and Doppler Frequency	29
2.7.1 Solving for the Complex Amplitude	30
III. MATLAB Simulations	32
3.1 Introduction	32
3.2 Methodology	32
3.3 Results	33
3.3.1 Metrics	33
3.3.2 Processing Time	34
3.3.3 SINR Loss	35
3.3.4 Power Spectral Density (PSD)	37
IV. Hardware Experiment	40
4.1 Introduction	40
4.2 Methodology	40
4.2.1 LFM Transmit Signal	40
4.2.2 Arbitrary Waveform Generator (AWG)	43
4.2.3 Transmit Antenna	43
4.2.4 Area of Interest	43
4.2.5 Phased Array	46
4.2.6 Oscilloscope	48
4.2.7 MATLAB Analysis	50
4.3 Results	54
4.3.1 Metrics	54
4.3.2 Power Spectral Density (PSD)	54
4.3.3 Matched Filter Response	55
V. Conclusions and Recommendations	60
5.1 Introduction	60
5.2 Conclusions	60
5.3 Recommendations	61
Bibliography	63

List of Figures

Figure	Page
2.1 I/Q detector	8
2.2 LFM matched filter response	11
2.3 STAP platform geometry	13
2.4 Data cube	14
2.5 Bistatic radar configuration	18
2.6 Local coordinate system with clutter patch	19
2.7 Monostatic STAP matched filter response	22
2.8 Power output	30
3.1 MATLAB simulation orientation	33
3.2 SINR loss	36
3.3 PSD of clutter ridge across range bins	39
4.1 Hardware experiment flow chart	41
4.2 Radar control GUI	41
4.3 Transmit antenna pattern	44
4.4 Overhead view of the hardware experiment	45
4.5 Picture of the hardware experiment	46
4.6 Diagram of phased array	48
4.7 Radiation pattern of the phased array	49
4.8 Picture of laboratory set up	50
4.9 Raw received signal	51
4.10 Matched filter response from hardware experiment	52
4.11 PSD of range bin with the LCD	57
4.12 PSD of the clutter ridge before and after the LCDR algorithm	58

Figure	Page
4.13 Down sampled matched filter response from the hardware experiment	59

List of Tables

Table	Page
3.1 Processing time	35
3.2 Relating RCS to CNR	35
3.3 Average SINR Loss for 100 trials	37

List of Symbols

Symbol	Definition
\mathbf{a}	temporal steering vector
α	complex amplitude
B	signal bandwidth (Hz)
\mathbf{b}	spatial steering vector
c	speed of light (m/s)
d	distance between channels (m)
\mathbf{E}	spectral energy
f_0	carrier frequency (Hz)
f_d	Doppler frequency (Hz)
f_r	pulse repetition frequency (Hz)
G_T	transmitter directional gain
g_R	element/subarray/channel directional gain
h	height (m)
$\hat{\mathbf{k}}$	line of sight unit vectors
L	number of range bins
L_D	bistatic baseline (m)
L_s	loss factor
M	number of pulses
N	number of channels
N_a	number of ambiguous range bins
N_c	number of discrete clutter patches in one range bin
P_T	transmitter power
R	range (m)

Symbol	Definition
\mathbf{R}	covariance matrix
ΔR	range resolution (m)
R_{ua}	unambiguous range (m)
ΔR_{LFM}	range resolution of LFM signal (m)
ΔT	round trip time to target (s)
T_r	pulse repetition interval (s)
\mathbf{v}	space-time steering vector
v_a	aircraft velocity (m/s)
\mathbf{w}	matched filter
x	complex radar return sample
\mathbf{x}	spatial snapshot ($N \times 1$)
$\bar{\mathbf{x}}$	space-time snapshot ($MN \times 1$)
\mathbf{X}	cell under test ($N \times M$)
β	bistatic angle (deg)
η	clutter ridge slope
γ	cone angle (deg)
λ_0	wavelength (m)
ω	normalized Doppler frequency
ϕ	azimuth angle (deg)
ϕ_{OP}	out-of-plane angle (deg)
ρ^2	noise power
σ	radar cross section
σ_0	clutter reflectivity coefficient
τ	pulse width (s)
τ_c	pulse width of chirp (s)

Symbol	Definition
θ	elevation angle (deg)
ϑ	normalized spatial frequency
ξ_R	single-pulse SNR for a single antenna element on receive

Subscripts

c	clutter
LCD	large clutter discrete
n	noise
R	receiver
t	target
T	transmitter

List of Acronyms

Acronym	Definition
APES	amplitude and phase estimation
AWG	arbitrary waveform generator
PBR	passive bistatic radar
CA-CFAR	cell averaging constant false alarm rate
CNR	clutter-to-noise ratio
CP	cyclic prefix
CPI	coherent processing interval
CUT	cell under test
DFT	discrete Fourier transform
DPO	digital phosphor oscilloscope
DVB-T	digital video broadcasting-terrestrial
GMTI	ground moving target indication
GSM	global system for mobile communications
GUI	graphical user interface
LCD	large clutter discrete
LCDR	LCD removal

Acronym Definition

LTE long-term evolution

LFM linear frequency modulation

OFDM orthogonal frequency division multiplexing

PRF pulse repetition frequency

PRI pulse repetition interval

PSD power spectral density

RAM radar absorbing material

RCS radar cross section

RF radio frequency

SINR signal-to-interference-plus-noise ratio

SMI sample matrix inversion

SNR signal-to-noise ratio

STAP space-time adaptive processing

STD standard deviation

ULA uniform linear array

AMPLITUDE ESTIMATION FOR THE LARGE CLUTTER DISCRETE REMOVAL ALGORITHM

I. Introduction

1.1 Introduction

Radar is an important technology used in both the civilian and military sectors to track and identify objects. Passive radar is a technique that uses signals already present in the environment (e.g., cell phone signals) and is becoming more popular as available radio frequency spectrum is getting more difficult to come by. An important part of all radar systems is distinguishing targets of interest from background noise or clutter. Clutter and noise impact the radar's ability to correctly track and identify targets. Signal processing techniques are used to attenuate this interference in order to increase the radar's probability of detection and decrease the probability of false alarm.

This research focuses on a signal processing algorithm that removes a spectrally bright localized scatterer called a large clutter discrete (LCD) from radar data. The technique, developed in [11], is called the LCD removal (LCDR) algorithm and can be broken into four steps:

1. Determine if a range bin has an LCD using a cell averaging constant false alarm rate (CA-CFAR) detector
2. Estimate the LCD's location in angle-Doppler with the Capon power estimator [2]
3. Estimate the complex amplitude of the LCD
 - (a) Use the amplitude and phase estimation (APES) technique [24] at the estimated angle-Doppler location for an initial guess

- (b) Finalize the complex amplitude estimate through an iterative process that minimizes the output power at a specific space-time location

4. Subtract the LCD from the data cube

This research focuses on step three, estimating the LCD's amplitude. Currently, the amplitude estimation takes two steps and involves an iterative process that can be slow and complicated. Additionally, this research will further verify the LCDR algorithm by developing and executing its first hardware experiment.

Removing clutter from the data increases the probability of detection for the radar system by improving the signal-to-interference-plus-noise ratio (SINR). Increasing the probability of detection improves the radar's ability to identify a target in an area of interest. Probability of detection is an important metric and impacts how well the user can accomplish the mission.

Previous research on LCD removal relies on a priori knowledge of the area of interest [13]. Typically, acquiring this information requires collecting data on the area and predicting clutter statistics. The LCDR algorithm increases operators' agility by eliminating a step in the collection process because no a priori knowledge is needed for the algorithm. Eliminating the need for a priori knowledge is useful for areas where it is difficult to conduct extra collections or time sensitive scenarios where estimating clutter statistics would slow the process down.

A potential impact from this signal processing algorithm is increased flexibility and resilience to conduct ground moving target indication (GMTI) to detect and track moving targets. Removing the requirement for a priori knowledge eliminates the time and effort required to collect information and estimate clutter characteristics on an area of interest. The LCDR algorithm could also enable operations in areas where it is difficult or impossible to estimate clutter characteristics. The LCDR algorithm can increase the agility of radar systems which supports broader Department of Defense missions and goals.

1.2 Problem Statement

This research will improve the LCD amplitude estimation step in the LCDR algorithm and evaluate the algorithm through MATLAB simulations and hardware experiments.

1.3 Scope

This research focuses on the amplitude estimation portion of the LCDR algorithm. This research will prove the LCD's complex amplitude can be estimated by minimizing the output power at the LCD's space-time location. This research will test this method through simulation and hardware experiments. This research will use all steps in the algorithm as outline in [11], but not investigate the accuracy or efficiency of steps one, two, or four.

1.4 Structure

Chapter 2 will provide background information on basic radar systems, space-time adaptive processing (STAP) systems, and clutter modeling. Previous research on clutter estimation techniques will be reviewed. Additionally, Chapter 2 will derive a method where the LCD's complex amplitude can be estimated in a closed form by minimizing the output the power at the LCD's space-time location.

Chapter 3 will provide the methodology and results for the MATLAB simulations. The results will be analyzed by comparing processing times between the grid search method and the new quadratic solution method. The results are also analyzed by calculating SINR loss and power spectral density (PSD).

Chapter 4 will cover the hardware experiments. There will be an in-depth explanation of each step in the experiment and the hardware components utilized. Next, the results are analyzed by calculated the PSD before and after the LCDR algorithm to assess how much of the LCD's energy is removed from the radar data.

Chapter 5 will outline conclusions and recommendations for future research. The conclusions drawn from the simulations and hardware experiments differ, but both show

the LCDR algorithm may be a promising method to remove LCDs from STAP data. For future research, the challenges and issues found during the hardware experiment should be modeled and their impact on the algorithm should be characterized.

II. Background

2.1 Introduction

Pulsed radar is a system that transmits a radio frequency (RF) electromagnetic pulse towards an area of interest and receives that pulse back when it is reflected off an object. Basic radar functions include detecting a target and determining the range. The range is the distance between the radar and object. Radar systems have transformed significantly from their early days. Modern radar systems can now track, identify, image, and classify targets while suppressing unwanted noise or clutter in the area of interest [18]. Clutter is defined as returns from any scatterers deemed to be not of tactical interest. Typical radar system components include a transmitter, antenna, receiver, and signal processor. This research focuses on the signal processor and techniques to eliminate clutter from the received data.

There are many different types of radar systems with variations on the location of transmitter and receiver and associated processing techniques to best suit the goal of each system. This research is focused on ground-facing air-borne radar used for detecting moving targets. This type of detection is called GMTI. One issue that arises with moving platforms is that Doppler is induced on the ground clutter. This makes it difficult to distinguish actual moving targets from ground clutter. STAP is a signal processing technique specialized for GMTI from airborne platforms. STAP, through adaptive digital beam forming, is able to detect moving targets by suppressing the Doppler induced clutter [17].

LCDs are localized and spectrally bright returns from clutter. Typical STAP systems attenuate homogeneous clutter by assuming the clutter is similar across the area of interest. An LCD causes the clutter to be heterogeneous. Heterogeneous clutter can not be attenuated through typical clutter suppression techniques because the clutter varies throughout the area of interest [17].

This research extends on the LCDR algorithm developed by Lievsay and Goodman which removes the LCD from the data [11]. The LCDR algorithm has four steps. The first step is to detect and estimate which range bin contains the LCD. Step one is accomplished by using a CA-CFAR detector. Step two estimates the LCD's location in angle-Doppler frequency using Capon power estimation [2]. Step three estimates the LCD's amplitude by using APES amplitude estimation [8] and some additional iterative processing that minimizes the power output at a specific space-time location. The last step is to remove the LCD from the data.

The following sections will provide an overview of basic monostatic radar systems, STAP topics to include passive bistatic radar (PBR) and clutter modeling, and previous research into clutter suppression techniques. There will be a full explanation of each step of the LCDR algorithm. The last section covers a new technique to estimate the LCD's complex amplitude to improve step three of the LCDR algorithm.

2.2 Radar

A monostatic radar configuration is defined as when the transmitter and receiver are collocated. A monostatic configuration is not relevant to PBR, but it will help provide a background on STAP systems. The monostatic radar equations can be modified for passive radar.

Consider a single transmitted pulse and a single point target at distance R from a monostatic radar. The round trip time, ΔT , from the transmitter/receiver to the target is

$$\Delta T = \frac{2R}{c}, \quad (2.1)$$

where c is the speed of light. Transmitting pulses separated by a fixed pulse repetition interval (PRI), T_r , is called a pulse train. The number of transmit/receive cycles in one second is the pulse repetition frequency (PRF), f_r . The duration of the pulse, in seconds, is

the pulse width, τ . The coherent processing interval (CPI), or dwell time, is the number of pulses multiplied by the PRI.

Radar data is often organized by pulse and range bin. For a simple radar pulse, range bins are determined by the range resolution,

$$\Delta R = \frac{c\tau}{2}, \quad (2.2)$$

and the unambiguous range,

$$R_{ua} = \frac{c}{2f_r}. \quad (2.3)$$

The unambiguous range is the maximum range at which a target can be measured unambiguously by the radar.

Matched filtering is often used to detect a target in the received data. The matched filter is the optimum linear filter that maximizes the signal-to-noise ratio (SNR). The received signal is correlated with the known transmitted signal to identify the time delay, which is then used to solve for the range using (2.1).

2.2.1 Linear Frequency Modulation (LFM) Pulse Signal Model.

A common radar waveform is a linear frequency modulation (LFM) pulse. An LFM pulse is used in the hardware experiments covered in Chapter 4. An LFM up chirp is a signal linearly swept in frequency from f_{min} to f_{max} [17]. The bandwidth, B , of the chirp is $B = f_{max} - f_{min}$. The pulse width of the chirp pulse is τ_c . A rectangular envelope is used to turn the pulse on and off to achieve the PRI. The rectangle envelope applied to the pulse is

$$b(t) = \begin{cases} 1 & 0 \leq t \leq \tau_c \\ 0 & \textit{else.} \end{cases} \quad (2.4)$$

At baseband, the LFM pulse is expressed as

$$s_{bb}(t) = b(t) \cos\left(\pi \frac{B}{\tau_c} t^2\right). \quad (2.5)$$

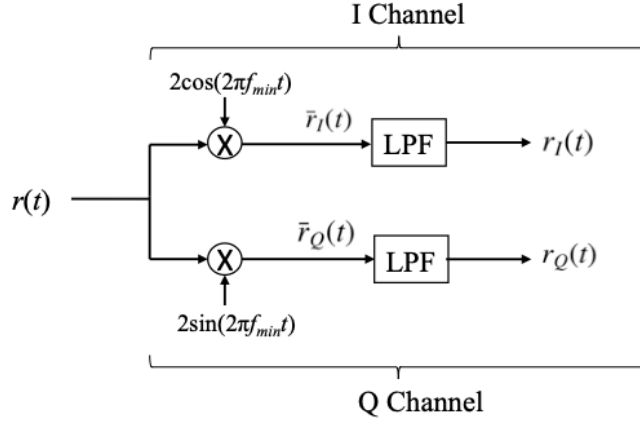


Figure 2.1: Two-channel I/Q detector that down converts and splits the received pulse into the in-phase and quadrature channels.

When transmitted, the LFM waveform is centered on the carrier frequency, which is f_{min} . The modulated transmit signal is

$$\begin{aligned}
 s(t) &= \text{Re} \{ s_{bb}(t) \exp(j2\pi f_{min} t) \} \\
 &= b(t) \cos \left(2\pi f_{min} t + \pi \frac{B}{\tau_c} t^2 \right).
 \end{aligned} \tag{2.6}$$

The received signal, $r(t)$, is a time delayed, ΔT , copy of the transmitted signal with some change in amplitude, A ,

$$r(t) = A s(t - \Delta T). \tag{2.7}$$

For this exercise, let $\Delta T = 0$. The received signal can be down converted and split into the in-phase and quadrature channels using the two-channel I/Q detector in Figure 2.1. The

demodulated signal from the I channel is

$$\begin{aligned}
\bar{r}_I(t) &= Ab(t) \cos\left(2\pi f_{min}t + \pi \frac{B}{\tau_c} t^2\right) 2 \cos(2\pi f_{min}t) \\
&= Ab(t) \left[\cos\left(2\pi f_{min}t + \pi \frac{B}{\tau_c} t^2 + 2\pi f_{min}t\right) + \cos\left(2\pi f_{min}t + \pi \frac{B}{\tau_c} t^2 - 2\pi f_{min}t\right) \right] \\
&= Ab(t) \left[\cos\left(4\pi f_{min}t + \pi \frac{B}{\tau_c} t^2\right) + \cos\left(\pi \frac{B}{\tau_c} t^2\right) \right], \tag{2.8}
\end{aligned}$$

and from the Q channel is

$$\begin{aligned}
\bar{r}_Q(t) &= Ab(t) \cos\left(2\pi f_{min}t + \pi \frac{B}{\tau_c} t^2\right) 2 \sin(2\pi f_{min}t) \\
&= Ab(t) \left[\sin\left(2\pi f_{min}t + \pi \frac{B}{\tau_c} t^2 + 2\pi f_{min}t\right) - \sin\left(2\pi f_{min}t + \pi \frac{B}{\tau_c} t^2 - 2\pi f_{min}t\right) \right] \\
&= Ab(t) \left[\sin\left(4\pi f_{min}t + \pi \frac{B}{\tau_c} t^2\right) - \sin\left(\pi \frac{B}{\tau_c} t^2\right) \right]. \tag{2.9}
\end{aligned}$$

Next, the signals are passed through a low pass filter to remove the copies at higher frequencies. The output for the I channel is

$$r_I(t) = Ab(t) \cos\left(\pi \frac{B}{\tau_c} t^2\right) \tag{2.10}$$

and for the Q channel is

$$r_Q(t) = -Ab(t) \sin\left(\pi \frac{B}{\tau_c} t^2\right). \tag{2.11}$$

The baseband complex received signal is

$$\begin{aligned}
r_{bb}(t) &= r_I(t) - jr_Q(t) \\
&= Ab(t) \cos\left(\pi \frac{B}{\tau_c} t^2\right) + jAb(t) \sin\left(\pi \frac{B}{\tau_c} t^2\right) \\
&= Ab(t) \exp\left(j\pi \frac{B}{\tau_c} t^2\right). \tag{2.12}
\end{aligned}$$

The baseband matched filter is

$$h_{bb}(t) = s^*(-t) = b(-t) \exp\left(-j\pi \frac{B}{\tau_c} t^2\right), \tag{2.13}$$

which is the time-reversed conjugate of the transmit signal. Now apply the matched filter to the received signal:

$$\begin{aligned}
y(t) &= r_{bb}(t) * h_{bb}(t) \\
&= \int_{-\infty}^{\infty} r_{bb}(\zeta) h_{bb}(t - \zeta) d\zeta \\
&= \int_{-\infty}^{\infty} Ab(\zeta) \exp\left(j\pi \frac{B}{\tau_c} \zeta^2\right) b(-(t - \zeta)) \exp\left(-j\pi \frac{B}{\tau_c} (t - \zeta)^2\right) d\zeta \\
&= A \int_{t-\tau_c}^{\tau_c} \exp\left(j\pi \frac{B}{\tau_c} (\zeta^2 - (t - \zeta)^2)\right) d\zeta, \quad |t| \leq \tau_c \\
&= A \int_{t-\tau_c}^{\tau_c} \exp\left(j\pi \frac{B}{\tau_c} (-t^2 + 2t\zeta)\right) d\zeta, \quad |t| \leq \tau_c.
\end{aligned} \tag{2.14}$$

From [17], (2.14) simplifies as,

$$y(t) = \left(1 - \frac{|t|}{\tau_c}\right) \frac{\sin\left[\left(1 - \frac{|t|}{\tau_c}\right)\pi B t\right]}{\left(1 - \frac{|t|}{\tau_c}\right)\pi B t}, \quad |t| \leq \tau_c. \tag{2.15}$$

The first term of the matched filter response in (2.15) is a triangle function defined over $-\tau_c < t < \tau_c$. The second term resembles a sinc function. Figure 2.2 shows (2.15) evaluated for $B = 0.3$ GHz and $\tau_c = 0.5 \mu\text{s}$. The peak of the matched filter response corresponds to the delay, ΔT , in the received signal. With $\Delta T = 0$, (2.15) also represents the ambiguity function with no uncompensated Doppler frequency shift. Ambiguity functions can be used to characterize the matched filter response in the presence of uncompensated Doppler shift from a moving scatterer [18].

An LFM signal is used for the hardware experiment and the matched filter response is calculated for each pulse and phased array channel. The matched filter responses are used to build the data cube, which is introduced in Section 2.3. The peak of the matched filter is used to determine the range of the LCD using (2.1).

The LFM signal is a pulse compressed signal. Pulse compression is a technique used to improve the range resolution while maintaining the energy desired in the pulse. As seen in (2.2), the range resolution for a simple radar pulse can only be improved by shortening

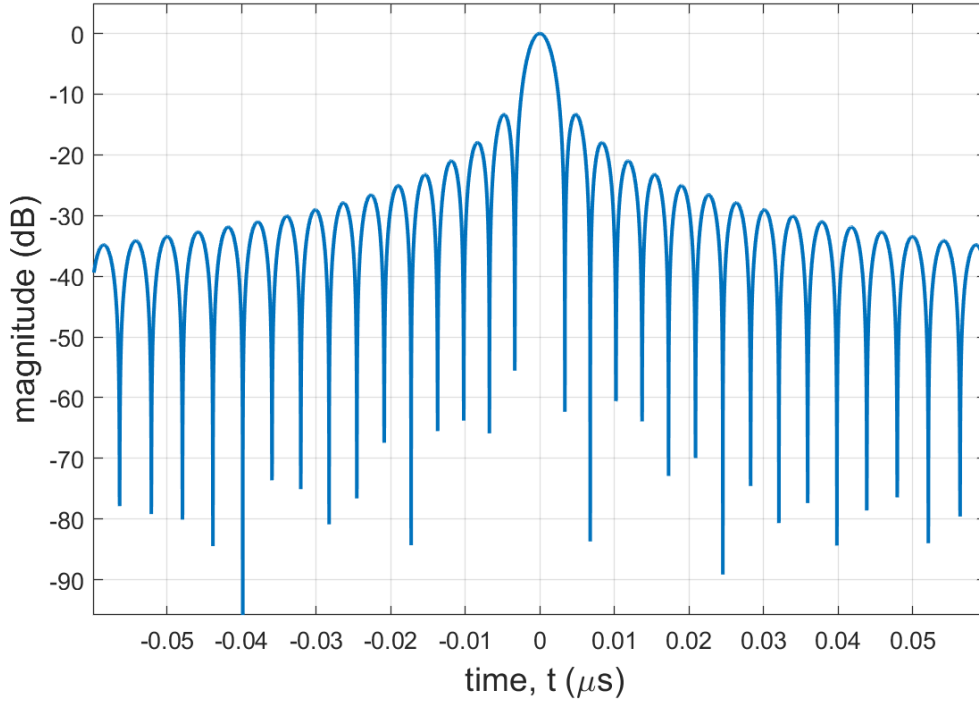


Figure 2.2: Matched filter response from (2.15) for LFM signal with $B = 0.3\text{GHz}$ and $\tau_c = 0.5\mu\text{s}$ with $\Delta T = 0$.

the pulse width. However, a shorter pulse width reduces the pulse's Doppler resolution and average signal power [18]. The range resolution for an LFM waveform is

$$\Delta R_{LFM} = \frac{c}{2B}, \quad (2.16)$$

which does not rely on the pulse duration.

A parameter that does rely on the pulse duration is the time-bandwidth product, $B\tau$, which is related to the LFM pulse compression gain [17]. The pulse compression gain is the ratio of the SNR at the output of the matched filter and the output prior to the filter [18]. The time-bandwidth product impacts the matched filter's ability to pull the signal out of the noise floor. For example, a longer transmit pulse can achieve improved SNR after the matched filter.

2.3 Space-Time Adaptive Processing (STAP)

STAP is a signal processing technique that suppresses clutter from radar returns to improve the probability of target detection in GMTI scenarios. If GMTI is performed from a stationary platform, STAP is not needed because the processor can easily attenuate clutter over all frequencies by filtering out any returns at a zero Doppler frequency. STAP becomes necessary when GMTI is performed from a moving platform and a range of Doppler frequencies are now induced on stationary clutter. Collecting echo returns signals from a phased array over a CPI (i.e. multiple pulses) enables STAP to filter data in multiple dimensions. STAP uses information from all the data collected to estimate the interference covariance matrix for clutter filtering.

2.3.1 Monostatic STAP Model.

This section will focus on a monostatic STAP model for an airborne radar system with a uniform linear array (ULA) and the bore-sight facing perpendicular to the direction of travel. Figure 2.3 shows the platform geometry with a ULA traveling parallel to the y-axis where v_a is the aircraft velocity. The point scatterer is shown in green and $\hat{\mathbf{k}}$ is the line of sight unit vector defined as

$$\hat{\mathbf{k}}(\phi, \theta) = \cos \theta \cos \phi \hat{\mathbf{x}} + \cos \theta \sin \phi \hat{\mathbf{y}} + \sin \theta \hat{\mathbf{z}}, \quad (2.17)$$

with θ and ϕ representing the elevation and azimuth angles, respectively.

The black dots on the ULA, in Figure 2.3, represent the channels and can be thought of as samples along the y-axis. The distance between adjacent channels is d . It is assumed each channel contains its own down converter, matched filter, and analog to digital converter. Additional radar system parameters include operating frequency, $\omega_0 = 2\pi f_0$, wavelength, λ_0 , PRI, T_r , and PRF, f_r .

Assuming N channels, M pulses, and L range bins, the received data from the ULA is organized into a data cube, \mathbf{D} , as illustrated by Figure 2.4. The complex sample for the m^{th}

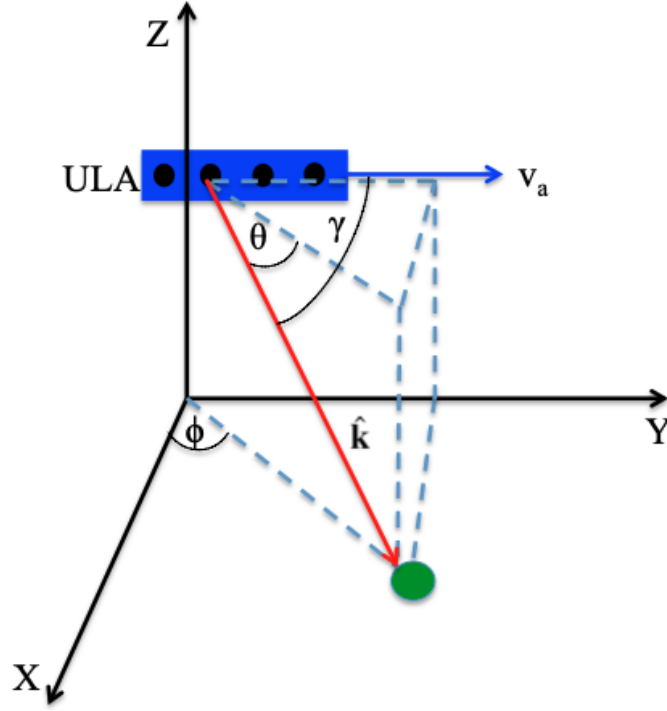


Figure 2.3: STAP platform geometry with a ULA traveling along the x-axis where \mathbf{v}_a is the aircraft velocity. The point scatterer is shown in green and the $\hat{\mathbf{k}}$ is the line of site unit vector with θ and ϕ representing the elevation and azimuth angles, respectively. The cone angle is represented with γ . The black dots on the ULA represent channels.

pulse, n^{th} channel, and l^{th} range bin is $x_{m,n,l}$. The spatial snapshot, $\mathbf{x}_{m,l}$, is an $N \times 1$ vector at the l^{th} range bin and m^{th} pulse. In STAP, there is a cell under test (CUT) that consists of all the data at one range bin. The data at some range bin l ,

$$\mathbf{X}_l = [\mathbf{x}_{1,l}, \mathbf{x}_{2,l}, \dots, \mathbf{x}_{M,l}]_{N \times M}, \quad (2.18)$$

can be described as a collection of all spatial snapshots over all pulses. The data outside the CUT is called the training data because it used to estimate the interference inside the CUT and train the adaptive filters. Another important data structure is the space-time snapshot,

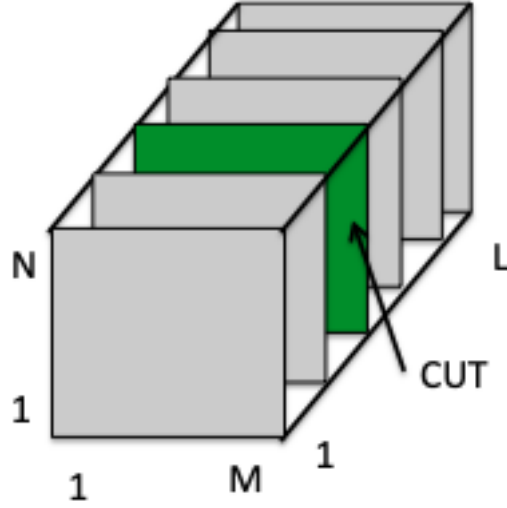


Figure 2.4: Data cube, \mathbf{D} , where N represents the number of channels, M the number of pulses in one CPI at a constant PRF, and L represents the number of range bins. The CUT is highlighted in green.

$\bar{\mathbf{x}}_l$, defined as

$$\bar{\mathbf{x}}_l = \text{vec}(\mathbf{X}_l) = [\mathbf{x}_{1,l}^T, \mathbf{x}_{2,l}^T, \dots, \mathbf{x}_{M,l}^T]^T_{MN \times 1}, \quad (2.19)$$

which is all the data at one range bin, l , organized in a vector.

The objective of the radar system is to determine if a target is present. The interference space-time snapshot at range bin l ,

$$\bar{\mathbf{x}}_{l,u} = \bar{\mathbf{x}}_{l,n} + \bar{\mathbf{x}}_{l,c}, \quad (2.20)$$

is made up of thermal noise, $\bar{\mathbf{x}}_{l,n}$, and clutter, $\bar{\mathbf{x}}_{l,c}$. Steering vectors are used to track phase changes between channels and pulses. Steering vectors digitally focus the array of antenna elements in a given direction or Doppler frequency by manipulating the phase shift for each pulse and/or channel [17]. The target's space-time steering vector is $\mathbf{v}(\vartheta_l, \omega_l)$, defined in (2.32), and the unknown complex amplitude of the target is α_l . Given a space-time snapshot

the system will make a hypothesis that either a target is absent,

$$H_0 : \bar{\mathbf{x}}_l = \bar{\mathbf{x}}_{l,u}, \quad (2.21)$$

or present,

$$H_1 : \bar{\mathbf{x}}_l = \alpha_t \mathbf{v}(\vartheta_t, \omega_t) + \bar{\mathbf{x}}_{l,u}. \quad (2.22)$$

Consider a clutter scatterer with parameters including range, R_c , azimuth, ϕ , elevation, θ , radar cross section (RCS), σ , and aircraft velocity, v_a . The induced Doppler frequency for a monostatic radar system at the clutter point is

$$f_d = \frac{2v_a}{\lambda_0} \cos \gamma, \quad (2.23)$$

where γ is the cone angle defined as the angle between the aircraft velocity vector and the line-of-site vector to a scatterer. The cone angle can be decomposed into the azimuth and elevation angles as follows:

$$\cos \gamma = \cos \theta \sin \phi. \quad (2.24)$$

The normalized Doppler frequency is

$$\omega = f_d T_r = \frac{f_d}{f_r}. \quad (2.25)$$

The normalized spatial frequency is

$$\vartheta = \frac{d}{\lambda_0} \cos \theta \sin \phi. \quad (2.26)$$

With the assumption of a ULA and constant f_r , the target samples can be expressed as

$$x_{nm} = \alpha_t e^{jn2\pi\vartheta} e^{jm2\pi\omega}, \quad (2.27)$$

where $n = 0, \dots, N - 1$ and $m = 0, \dots, M - 1$. For monostatic STAP systems, the elevation angle is constant within a single range bin. In one range bin, the system is looking for targets at different azimuth angles and Doppler frequencies. The spatial steering vector is

$$\mathbf{a}(\phi, \theta) = \left[1, e^{j\frac{2\pi d}{\lambda_0} \cos \theta \sin \phi}, \dots, e^{j(N-1)\frac{2\pi d}{\lambda_0} \cos \theta \sin \phi} \right]_{N \times 1}^T. \quad (2.28)$$

Equation (2.28) can be simplified using (2.26) which results in

$$\mathbf{a}(\vartheta) = \left[1, e^{j2\pi\vartheta}, \dots, e^{j(N-1)2\pi\vartheta} \right]_{N \times 1}^T. \quad (2.29)$$

Equation (2.29) describes the phase relationship from channel to channel and depends on the element spacing, d , and the angle of arrival [17]. The temporal steering vector is

$$\mathbf{b}(\phi, \theta) = \left[1, e^{j2\pi \frac{2v_a}{\lambda_0 f_r} \cos \theta \sin \phi}, \dots, e^{j(M-1)2\pi \frac{2v_a}{\lambda_0 f_r} \cos \theta \sin \phi} \right]_{M \times 1}^T. \quad (2.30)$$

Equation (2.30) can be simplified using (2.23) and (2.24) which results in

$$\mathbf{b}(\omega) = \left[1, e^{j2\pi\omega}, \dots, e^{j(M-1)2\pi\omega} \right]_{M \times 1}^T. \quad (2.31)$$

Equation (2.31) tracks the phase change from pulse to pulse and depends on the Doppler frequency. This assumes a uniform PRF and constant aircraft velocity over the CPI. The space-time steering vector is

$$\mathbf{v}(\vartheta, \omega) = \mathbf{b}(\omega) \otimes \mathbf{a}(\vartheta) \quad (MN \times 1), \quad (2.32)$$

where \otimes is the Kroncker product.

STAP systems detect a target and estimate its associated spatial and Doppler frequencies. The space-time matched filter that maximizes SINR is

$$\mathbf{w} = \kappa \mathbf{R}_u^{-1} \mathbf{v}(\hat{\vartheta}, \hat{\omega}), \quad (2.33)$$

where κ is an arbitrary constant and $\mathbf{R}_u = \mathbb{E} \left[\bar{\mathbf{x}}_u \bar{\mathbf{x}}_u^H \right]$ is the interference covariance matrix.

2.3.2 *Passive Bistatic Radar (PBR).*

Radar that uses signals already present in the environment to detect and identify targets is called PBR. The system is bistatic because the transmitter and receiver are on different platforms. One advantage of passive radar is no money or resources need to be spent on the transmitter. Additionally, it is not necessary to secure an RF license to transmit. However, there are challenges associated with passive radar. The radar designer does

not have control over the waveform design, including frequency, power, and pulse width. Additionally, radar users have no control over where the transmitters are located which may cause high clutter spectrum energy and reduce the system's probability of detection. However, these challenges can be addressed through antenna design, a priori knowledge, or post processing. PBR is a useful option for many scenarios.

Waveforms for PBR are assumed to be generated by non-cooperative systems. A variety of commercial signals have been researched including digital video broadcasting-terrestrial (DVB-T) [5, 14–16, 21–23], global system for mobile communications (GSM) [12], and long-term evolution (LTE) signals [1, 3, 19]. All the commercial signals listed above are continuous communication waveforms. Assuming a separable direct path signal exists, a PBR system can apply the pulse envelope from (2.4) every T_r seconds to generate pulse-diverse waveforms. Pulse-diverse waveforms mean each pulse differs by some combination of phase, phase code, time offset, and/or frequency shift [20].

For this PBR model, the receiver is an airborne side-looking radar and the transmitter is stationary. The height of the receiver and transmitter are h_R and h_T , respectively, where $h_R > h_T$. The elevation angle, θ_T , is the angle from the receiver to the transmitter, as seen in Figure 2.5. The distance between the transmitter and receiver is called the bistatic baseline, L_D , and calculated as

$$L_D = \left| \frac{h_R - h_T}{\sin \theta_T} \right|. \quad (2.34)$$

In the x-y plane, the azimuth angle, ϕ_T , is defined as the angle between the transmitter and receiver and behaves according to the right hand rule with zero degrees on the x-axis. In a global axis, the receiver is at $(0, 0, h_R)$ and the transmitter is at $(L_D \cos \theta_T \cos \phi_T, L_D \cos \theta_T \sin \phi_T, h_T)$. The distances between the transmitter and receiver to any point on the ground are R_T and R_R , respectively. The angle between the range

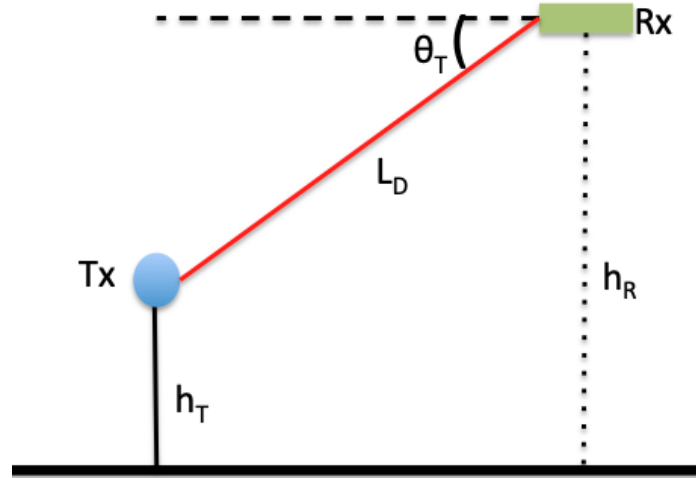


Figure 2.5: Transmitter (Tx) and receiver (Rx) configuration in the x - z plane where h_T is the Tx height, h_R is the Rx height, L_D is the bistatic baseline, and θ_T is the elevation angle between the Tx and Rx.

vectors, \vec{R}_T and \vec{R}_R , is the bistatic angle, β ,

$$\beta = \cos^{-1} \left(\frac{\vec{R}_T \cdot \vec{R}_R}{R_T R_R} \right). \quad (2.35)$$

The bistatic range, R_B ,

$$R_B = R_T + R_R, \quad (2.36)$$

is the total distance from the transmitter to a point on the ground to the receiver.

2.3.3 Passive STAP Clutter Model.

Clutter contributions from the l^{th} range bin are the continuous sum of voltage responses from all scatterers within the l^{th} range bin and any ambiguous range bins [27]. The continuous sum can be approximated as

$$\mathbf{c}_l = \sum_{j=1}^{N_a} \sum_{i=1}^{N_c} \alpha_{ijk} \bar{\mathbf{x}}(\vartheta_{ijl}, \omega_{ijl}), \quad (2.37)$$

where N_a is the number of ambiguous range bins, N_c is the number of discrete clutter patches in one range bin, and α_{ijl} is the random reflection coefficient of the $(i^{\text{th}}, j^{\text{th}}, l^{\text{th}})$ clutter patch. The clutter patch's power, ξ_{ijl} , is defined using the bistatic range equation

$$\xi_{ijl} = \frac{P_T G_T g_R \lambda_0^2 \sigma_{ijl}}{(4\pi)^3 L_s R_T^2 R_R^2}, \quad (2.38)$$

where P_T is the transmitter power, G_T is the transmitter directional gain, g_R is the element/subarray/channel directional gain, L_s is the loss factor, and σ_{ijl} is the clutter patch RCS. The clutter patch's RCS is modeled as

$$\sigma_{ijl} = \sigma_0(\theta_I, \theta_S, \phi_{OP}) A_{ijl}, \quad (2.39)$$

where A_{ijl} is the area of the $(i^{\text{th}}, j^{\text{th}}, l^{\text{th}})$ clutter patch and σ_0 is the clutter patch reflectivity coefficient with $(\theta_I, \theta_S, \phi_{OP})$ shown in Figure 2.6.

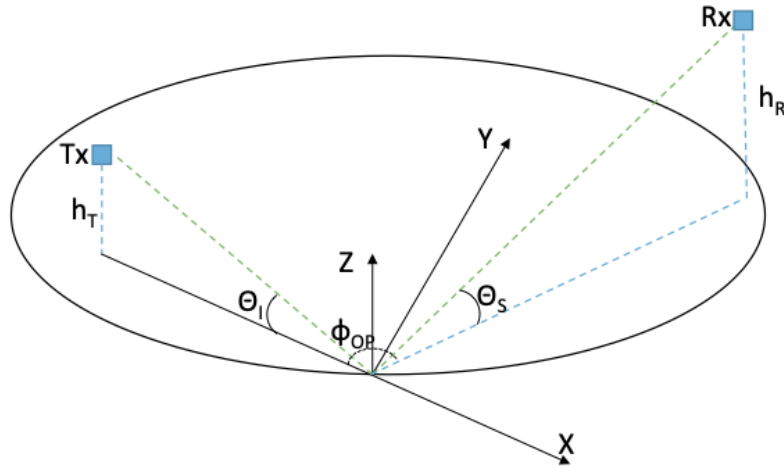


Figure 2.6: The reflectivity coefficient is defined by θ_I , θ_S , and ϕ_{OP} using a local coordinate system with the clutter patch at the origin and the transmitter on the x-axis.

The reflectivity coefficient is a function of $(\theta_I, \theta_S, \phi_{OP})$ because σ_0 is strongly dependent on relative geometry [10]. The out-of-plane angle, ϕ_{OP} , has the greatest impact

on the RCS coefficient [10]. When $\phi_{OP} = 0^\circ$ (back scattering) and $\phi_{OP} = 180^\circ$ (forward scattering), σ_0 is at its strongest. When $\phi_{OP} = 90^\circ$, σ_0 is at its weakest. The clutter structure in the spatial/Doppler frequency domain depends on the relative geometry of the transmitter and receiver.

One disadvantage with bistatic radar is that the clutter is inherently non-stationary because the clutter statistics are range dependent [10]. The bistatic range, from (2.36), within a single range bin is the same, but R_T and R_R will vary for each clutter scatterer. The varying R_T and R_R impact the clutter patch's power, as seen in (2.38), which results in the clutter being inherently range dependent. Therefore, clutter in the training data may not be representative of the clutter in the CUT. Clutter is often assumed to be range independent for monostatic radar. Non-stationary clutter reduces the effectiveness of clutter suppression.

In the passive STAP system, the transmitter is stationary and the receiver is mounted onto an airborne platform in a side looking configuration. The airborne platform induces Doppler shifts on the clutter scene. However, the induced Doppler shifts are half that of a monostatic system with a moving transmitter and receiver. The induced Doppler shifts are defined by

$$f_d = \frac{\hat{\mathbf{k}}_{R_x} \cdot \mathbf{v}_{R_x} + \hat{\mathbf{k}}_{T_x} \cdot \mathbf{v}_{T_x}}{\lambda_0}, \quad (2.40)$$

where $\hat{\mathbf{k}}_{R_x}$ and $\hat{\mathbf{k}}_{T_x}$ are unit vectors that represent the line of sight from the transmitter and receiver to a point on the ground and \mathbf{v}_{R_x} and \mathbf{v}_{T_x} represent the receiver and transmitter velocity vectors. For a monostatic system, $\hat{\mathbf{k}}_{T_x} = \hat{\mathbf{k}}_{R_x}$ and $\mathbf{v}_{T_x} = \mathbf{v}_{R_x}$, so (2.40) simplifies to (2.23). In a passive bistatic radar system, $\mathbf{v}_{T_x} = 0$ and (2.40) simplifies to

$$\begin{aligned} f_d &= \frac{v_a}{\lambda_0} \cos \gamma \\ &= \frac{v_a}{\lambda_0} \cos \theta \sin \phi. \end{aligned} \quad (2.41)$$

The normalized Doppler shift for a clutter patch, ω_c , is

$$\omega_c = \frac{v_a}{\lambda_0 f_r} \cos \theta \sin \phi. \quad (2.42)$$

The normalized spatial frequency for a clutter patch, ϑ_c , is

$$\vartheta_c = \frac{d}{\lambda_0} \cos \theta \sin \phi. \quad (2.43)$$

Using (2.42) and (2.43), the clutter patch's angle-Doppler response is a linear relationship defined as

$$\omega_c = \frac{v_a d}{\lambda_0 f_r d} \cos \theta \sin \phi = \frac{v_a}{f_r d} \vartheta_c. \quad (2.44)$$

2.3.4 Clutter Ridge.

In the normalized Doppler and spatial frequency domain, the clutter ridge slope is defined as

$$\eta = \frac{v_a}{f_r d}. \quad (2.45)$$

The clutter ridge relates where clutter energy resides in the spatial and Doppler domain. If $\eta = 1$, power from the clutter resides on the diagonal where spatial and Doppler frequency are equal. Figure 2.7 is the matched filter response for a monostatic STAP system when $\eta = 1$. The clutter ridge can be seen along the diagonal where there is high attenuation to filter out the clutter. When $\eta \neq 1$, aliasing can occur in the Doppler or spatial frequency domain. This creates more nulls in the matched filter angle/Doppler domain which make target detection more difficult.

2.4 Long-Term Evolution (LTE) Waveforms

LTE signals are a type of wireless telecommunication signal for mobile phones and can be utilized by PBR systems. The LTE waveform uses orthogonal frequency division multiplexing (OFDM) to organize data into 10 ms frames, 1 ms subframes, and 0.5 ms slots. Every slot contains six or seven symbols based on which cyclic prefix (CP) is chosen [3]. A CP is used to mitigate impacts from multipath by copying a portion of the end of the signal to the beginning on the signal.

The MATLAB simulations in this research use LTE signals as the passive emitter. For the simulations, a pulse is defined as one symbol with random simulated user data. This

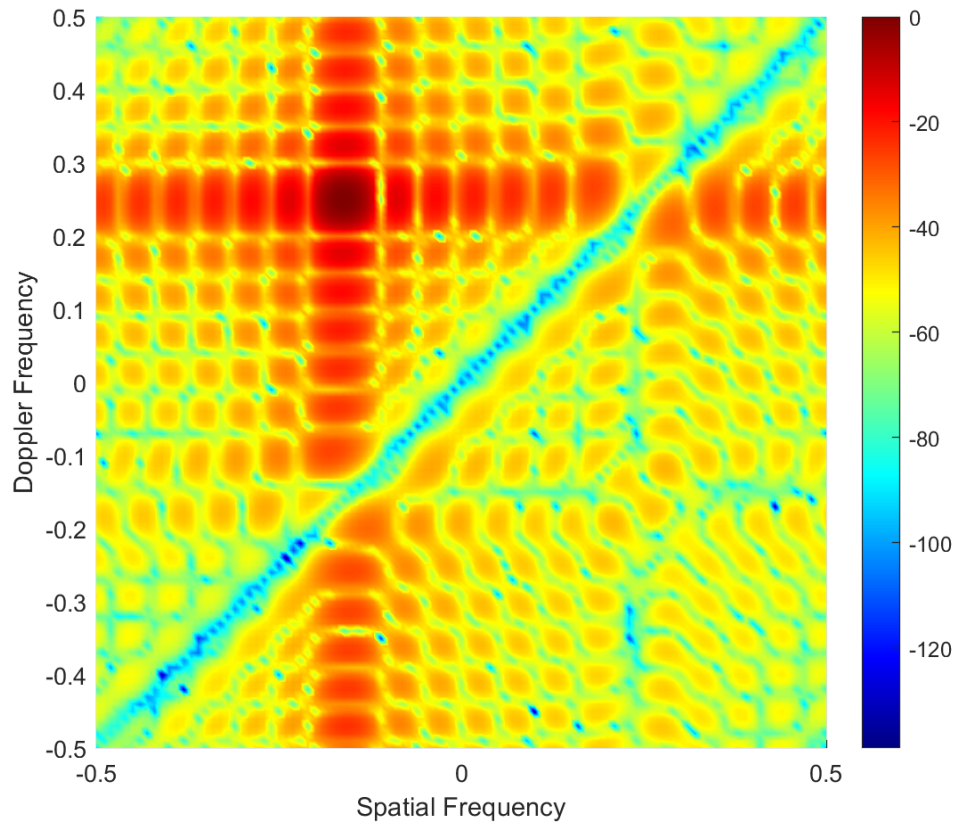


Figure 2.7: The matched filter response for a monostatic STAP system in dB when $\eta = 1$. The matched filter's passband is at $(\vartheta = -0.16, \omega = 0.25)$ and the clutter ridge is where $\vartheta = \omega$.

ensures the transmit signal is a pulse-diverse waveform. Similar to the LFM signal analysis in Section 2.2.1, the matched filter for an LTE signal is the time reverse conjugate of the transmit signal.

2.5 Previous Research on Clutter Suppression and LCD Removal

2.5.1 Homogeneous Clutter Suppression.

It is assumed homogeneous ground clutter exists over all azimuth angles and ranges and is attenuated through matched filtering. The estimated interference covariance matrix, $\hat{\mathbf{R}}_u$, can be calculated with sample matrix inversion (SMI), which is defined as

$$\hat{\mathbf{R}}_u = \frac{1}{L-1} \sum_{l=1}^{L-1} \bar{\mathbf{x}}_l \bar{\mathbf{x}}_l^H. \quad (2.46)$$

This method removes the CUT from the data cube and averages radar returns in the training data. If the CUT has the target and the training data is only radar returns from interference, $\hat{\mathbf{R}}_u$ can estimate the interference inside the CUT. In order for $\hat{\mathbf{R}}_u$ to be accurate, clutter outside the CUT must be similar to clutter inside the CUT. In other words, the clutter needs to be homogeneous. An LCD causes the clutter to be heterogeneous.

Ground clutter is attenuated with a matched filter that incorporates $\hat{\mathbf{R}}_u$. Maximizing SINR will maximize the probability of detection. The optimum matched filter that maximizes the probability of detection is

$$\mathbf{w}(\hat{\vartheta}_t, \hat{\omega}_t) = \kappa \hat{\mathbf{R}}_u^{-1} \mathbf{v}(\hat{\vartheta}_t, \hat{\omega}_t), \quad (2.47)$$

where $\hat{\vartheta}_t$ and $\hat{\omega}_t$ are the hypothesized target spatial and Doppler frequencies and κ is an arbitrary constant. The matched filter's passband is at the hypothesized target space-time frequency pair while simultaneously filtering out the coherent interference contained in $\hat{\mathbf{R}}_u$ (see Figure 2.7).

2.5.2 LCD Removal.

An LCD is a spectrally localized scatterer present in STAP data. Examples of objects that would appear as LCDs are large buildings in urban areas or grain silos in an open field. LCDs are localized and range dependent scatterers that may only show up in a single slice of the data cube. An LCD can impact performance of STAP in different ways depending on where the LCD is in the data. An LCD in the CUT could be interpreted as a target, which

would cause a false alarm. If the LCD is in the training data, the algorithm will be trained to null that space-time location and potentially miss a target in the CUT. It is advantageous to remove the LCD because false alarms and missed detections should be avoided.

The authors in [13] use prior knowledge about the area of interest to remove clutter from the STAP data. This method is called knowledge-aided STAP. The authors form earth-referenced clutter reflectivity maps and extract estimates of clutter return strength. The estimates are incorporated into a clutter map of the area of interest. To remove the LCD, the authors scan the estimated clutter map and use a threshold to determine if there is an LCD in that data set. Then they use the maximum likelihood method to determine the complex amplitude and azimuth angle.

The LCDR algorithm developed in [11] uses no prior knowledge to remove the LCD. This method is covered in Section 2.6.

2.6 LCDR Algorithm

The LCDR algorithm developed by Lievsay in [11] can be broken into four steps:

1. Determine if a range bin has an LCD using a cell averaging constant false alarm rate (CA-CFAR) detector
2. Estimate the LCD's location in angle-Doppler with the Capon power estimation [2]
3. Estimate the complex amplitude of the LCD
 - (a) Use APES technique [24] to the estimated angle-Doppler location to generate initial guesses and define a local search grid in the real and imaginary space
 - (b) Finalize the complex amplitude estimate through an iterative process that minimizes output power at the specific space-time location
4. Subtract the LCD from the data cube

2.6.1 Step One.

CA-CFAR detector is the method used to detect if an LCD is present in the data. CA-CFAR detectors are also used to detect targets. The detector compares the signal to an adaptive threshold to determine if an LCD is present. The null hypothesis, H_0 , is an LCD is not present and the alternative hypothesis, H_1 , is an LCD is present. The threshold is calculated from the arithmetic mean of the surrounding interference levels in range and spatial/Doppler frequency [9].

First, to detect an LCD and estimate the range bin, the spectral energy, \mathbf{E} , is calculated across the clutter ridge in each range bin, l , as

$$\mathbf{E}_l(\vartheta, \eta\vartheta) = |\mathbf{a}^H(\vartheta)\mathbf{X}_l^*\mathbf{b}(\eta\vartheta)|^2 \quad (2.48)$$

over a range of spatial frequencies normalized to -0.5 to 0.5. If there is an LCD, it will reside on the clutter ridge. Apply the CA-CFAR detector to \mathbf{E} .

The out-of-plane angle, ϕ_{OP} , from Figure 2.6, is an important parameter that gives insight as to whether the CA-CFAR detector will be able to detect the LCD. The CA-CFAR detector is unlikely to detect the LCD if $\phi_{OP} \approx 0^\circ$ or $\phi_{OP} \approx 180^\circ$ because the LCD return will reside in a spatial/Doppler area with high clutter energy [11]. In other words, the LCD will blend with the other clutter in the scene. Therefore, this LCDR algorithm is unlikely to work for monostatic STAP systems.

2.6.2 Step Two.

Step two in the LCDR algorithm involves estimating the spatial and Doppler frequencies of the LCD using the Capon frequency estimation technique described in [2]. The Capon method estimates the power spectrum by filtering a wide sense stationary process with a bank of narrowband bandpass filters [7]. The filters are adapted for each frequency of interest. The frequency that maximizes the output power corresponds to the relative angle between the ULA and the LCD.

First, the received data from one channel in the range bin with the LCD can be defined as $x[m]$. Let \mathbf{y}_k be a sub-sequence of length L_M of the received data, where k represents the k^{th} sub-sequence. Let \mathbf{Y} be a matrix of all possible sub-sequences such that

$$\mathbf{Y} = [\mathbf{y}_0, \dots, \mathbf{y}_{K-1}] = \begin{bmatrix} x[0] & x[1] & \dots & x[K-2] & x[K-1] \\ x[1] & x[2] & & x[K-1] & x[K] \\ \vdots & & \ddots & & \vdots \\ x[L_M-2] & x[L_M-1] & & x[M-3] & x[M-2] \\ x[L_M-1] & x[L_M] & \dots & x[M-2] & x[M-1] \end{bmatrix}, \quad (2.49)$$

where $K = M - L_M + 1$ is the total number of sub-sequences.

The covariance matrix of \mathbf{y}_k is $\mathbf{R} = E\{\mathbf{y}_k \mathbf{y}_k^H\}$. However, in practice \mathbf{R} must be estimated as

$$\hat{\mathbf{R}} = \frac{1}{K} \sum_{k=0}^{K-1} \mathbf{y}_k \mathbf{y}_k^H = \frac{1}{K} \mathbf{Y} \mathbf{Y}^H. \quad (2.50)$$

The estimated Doppler frequency is

$$\hat{\omega}_{LCD} = \operatorname{argmax}_{\omega} \frac{1}{\mathbf{b}_{L_M}^H(\omega) \hat{\mathbf{R}}^{-1} \mathbf{b}_{L_M}(\omega)}, \quad (2.51)$$

where \mathbf{b}_{L_M} is the temporal steering vector of length L_M .

Equation (2.51) can be extended to two dimensions to search for the Doppler and spatial frequency. Let us define a two-dimensional space-time series as $x[n, m]$. The sub-sequences are defined as

$$\mathbf{y}_{k_N, k_M} = \operatorname{vec} \left(\begin{bmatrix} x[k_N, k_M] & \dots & x[k_N, k_M + L_M - 1] \\ \vdots & \ddots & \vdots \\ x[k_N + L_N - 1, k_M] & \dots & x[k_N + L_N - 1, k_M + L_M - 1] \end{bmatrix} \right), \quad (2.52)$$

where L_N and L_M are the lengths of the subset of space and time samples taken from $x[n, m]$.

The number of unique windows in space and time are

$$K_N = N - L_N + 1 \quad (2.53)$$

and

$$K_M = M - L_M + 1, \quad (2.54)$$

respectively. Define \mathbf{Y} as

$$\mathbf{Y} = \begin{bmatrix} \mathbf{y}_{0,0} & \mathbf{y}_{1,0} & \cdots & \mathbf{y}_{K_N-1,0} & \mathbf{y}_{0,1} & \mathbf{y}_{1,1} & \cdots & \mathbf{y}_{K_N-1,K_M-1} \end{bmatrix}, \quad (2.55)$$

which collects the snapshots from (2.52) with different k_N and k_M .

The covariance matrix with the two-dimensional data is similar to (2.50), but is defined as

$$\hat{\mathbf{R}} = \frac{1}{K_N K_M} \mathbf{Y} \mathbf{Y}^H. \quad (2.56)$$

Therefore, the spatial and Doppler frequency can be estimated using

$$[\hat{\vartheta}_{LCD}, \hat{\omega}_{LCD}] = \underset{\vartheta, \omega}{\operatorname{argmax}} \frac{1}{\mathbf{v}_{L_N, L_M}^H(\vartheta, \omega) \hat{\mathbf{R}}^{-1} \mathbf{v}_{L_N, L_M}(\vartheta, \omega)}. \quad (2.57)$$

Let $\mathbf{v}_{L_N, L_M}(\vartheta, \omega)$ represent a space-time steering vector such that

$$\mathbf{v}_{L_N, L_M}(\vartheta, \omega) = \left[1, e^{j2\pi\omega}, \dots, e^{j2\pi\omega(L_N-1)} \right] \otimes \left[1, e^{j2\pi\vartheta}, \dots, e^{j2\pi\vartheta(L_M-1)} \right], \quad (2.58)$$

where \otimes is the Kronecker product. However, the LCD's spatial and Doppler frequency are related through the clutter ridge and (2.44). Therefore, the one-dimensional analysis can be sufficient.

2.6.3 Step Three.

This research focuses on step three, estimating the LCD's complex amplitude, α . The original steps in [11] estimate the complex amplitude in two parts. First, APES technique [6, 8] is used to attain an initial guess of the complex amplitude. Then, the amplitude estimate is finalized through an iterative process that minimizes the output power at a $(\vartheta_{LCD}, \omega_{LCD})$.

For a two-dimensional frequency spectrum, the estimated complex amplitude is defined as

$$\hat{\alpha}_{APES} = \frac{\mathbf{v}_{L_N, L_M}^H(\vartheta, \omega) \hat{\mathbf{Q}}^{-1}(\vartheta, \omega) \mathbf{g}(\vartheta, \omega)}{\mathbf{v}_{L_N, L_M}^H(\vartheta, \omega) \hat{\mathbf{Q}}^{-1}(\vartheta, \omega) \mathbf{v}_{L_N, L_M}(\vartheta, \omega)}, \quad (2.59)$$

where $\hat{\mathbf{R}}$ is from (2.56) and

$$\hat{\mathbf{Q}}(\vartheta, \omega) = \hat{\mathbf{R}} - \mathbf{g}(\vartheta, \omega)\mathbf{g}^H(\vartheta, \omega). \quad (2.60)$$

Additionally, $\mathbf{g}(\vartheta, \omega)$ is defined as

$$\mathbf{g}(\vartheta, \omega) = \frac{1}{K_N K_M} \sum_{k_n=0}^{K_N-1} \sum_{k_m=0}^{K_M-1} \mathbf{y}_{k_n, k_m} e^{j(\vartheta k_n + \omega k_m)}. \quad (2.61)$$

It was found in [11] that the APES estimation was not accurate enough to successfully remove the LCD. Therefore, multiple complex amplitude estimates are generated through the APES method by varying the sub-sequence length. The statistical outliers are removed and the rest of the estimates are used to create a search space in the real and imaginary domain. A linearly spaced search grid of 25 by 25, with the limits set by the estimates, is used to find the local minimum of

$$S = \mathbf{v}^H \text{vec}\{\mathbf{X}_l - \hat{\alpha}\mathbf{ab}^T\} \text{vec}\{\mathbf{X}_l - \hat{\alpha}\mathbf{ab}^T\}^H \mathbf{v}. \quad (2.62)$$

Equation (2.62) calculates the output power at the estimated spatial and Doppler frequencies from step two. The data cube slice at the range bin with the LCD is \mathbf{X}_l and the complex amplitude estimate is $\hat{\alpha}$. The amplitude estimate that minimizes (2.62) is used to generate a finer search grid and the process is repeated. This iterative approach continues until the output power is below a chosen threshold and the amplitude estimate is considered accurate enough to remove the LCD from the data. This research focuses on improving this step because it is slow and complicated.

2.6.4 Step Four.

Once the LCD's spatial and Doppler frequencies and complex amplitude are estimated, it can be subtracted from the data cube. The LCD has side lobes that extend across range bins which must be accounted for in the subtraction. To account for the side lobes, the normalized auto-correlation function of the transmit signal, \mathbf{R}_{XX} , is used. The auto-correlation function will be an $(N \times M \times L)$ array with the peak centered at the range

bin with the LCD and $\mathbf{R}_{XX,l}$ represents an $(N \times M)$ matrix at range bin l . The new data cube is constructed by subtracting the LCD from each range bin,

$$\mathbf{X}'_l = \mathbf{X}_l - \hat{\alpha} \left(\mathbf{a}(\hat{\vartheta}_{LCD}, \hat{\omega}_{LCD}) \mathbf{b}(\hat{\vartheta}_{LCD}, \hat{\omega}_{LCD})^T \right) \odot \mathbf{R}_{XX,l}, \quad (2.63)$$

where \odot is the Hadamard or piece-wise product.

2.7 Output Power at a Spatial and Doppler Frequency

Assume a STAP system has N channels, M pulses, and L range bins. The output power at $\hat{\vartheta}_{LCD}$ and $\hat{\omega}_{LCD}$ frequencies is

$$S = \mathbf{v}^H(\hat{\vartheta}_{LCD}, \hat{\omega}_{LCD}) \text{vec}\{\mathbf{X}_l\} \text{vec}\{\mathbf{X}_l\}^H \mathbf{v}(\hat{\vartheta}_{LCD}, \hat{\omega}_{LCD}), \quad (2.64)$$

where \mathbf{X}_l ($N \times M$) is the STAP data cube slice at the l^{th} range bin with the LCD. Equation (2.64) can be used to estimate the LCD's complex amplitude, α , by finding the amplitude that minimizes the power output at the LCD's estimated spatial and Doppler frequency. Minimizing the output power with respect to α will find the value that eliminates the most power associated with the LCD, therefore, finding the best estimate of the complex amplitude. The LCD's complex amplitude, α , is multiplied by spatial and temporal steering vectors and subtracted from the data cube to remove all the power associated with the LCD, thus

$$S = \mathbf{v}^H(\hat{\vartheta}_{LCD}, \hat{\omega}_{LCD}) \text{vec}\{\mathbf{X}_l - \alpha \mathbf{a}(\hat{\vartheta}_{LCD}) \mathbf{b}(\hat{\omega}_{LCD})^T\} \text{vec}\{\mathbf{X}_l - \alpha \mathbf{a}(\hat{\vartheta}_{LCD}) \mathbf{b}(\hat{\omega}_{LCD})^T\}^H \mathbf{v}(\hat{\vartheta}_{LCD}, \hat{\omega}_{LCD}). \quad (2.65)$$

The spatial and Doppler frequency have already been estimated in step two of the LCDR algorithm.

Figure 2.8 shows (2.65) evaluated over multiple α 's in the real and imaginary space and converted to dB. Equation (2.65) trends towards the minimum as α reaches the true value of the LCD's amplitude.

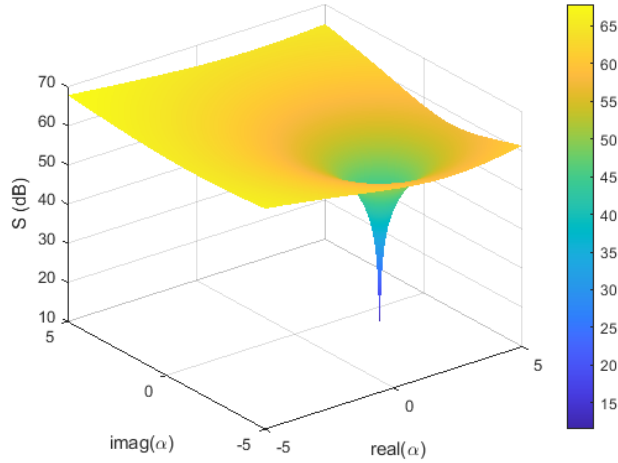


Figure 2.8: Power output, (2.65), evaluated over multiple α 's in the real and imaginary space.

2.7.1 Solving for the Complex Amplitude.

The derivation described in this section is a product of this research. It was discovered that directly solving for the amplitude that minimizes the output power at the LCD's space-time location produces an accurate amplitude estimate. Therefore, there is no longer a need for the initial guesses from the APES estimation.

Equation (2.65) defines the output power at the LCD's spatial and Doppler frequency. The α that minimizes the power output is the best estimate of the complex amplitude:

$$\hat{\alpha} = \underset{\alpha}{\operatorname{argmin}} S = \underset{\alpha}{\operatorname{argmin}} \mathbf{v}^H \operatorname{vec}(\mathbf{X}_l - \alpha \mathbf{a} \mathbf{b}^T) \operatorname{vec}(\mathbf{X}_l - \alpha \mathbf{a} \mathbf{b}^T)^H \mathbf{v}. \quad (2.66)$$

For Section 2.7.1, assume all the steering vectors are steered to $(\hat{\vartheta}_{LCD}, \hat{\omega}_{LCD})$.

Equation (2.65) can be written in matrix form and expanded into summations, as follows:

$$\begin{aligned}
S &= \sum_{i=1}^{MN} \sum_{j=1}^{MN} v_i^* \left(\text{vec}(\mathbf{X}_l)_i - \alpha \text{vec}(\mathbf{ab}^T)_i \right) \left(\text{vec}^*(\mathbf{X}_l)_j - \alpha^* \text{vec}^*(\mathbf{ab}^T)_j \right) v_j \\
&= \sum_{i=1}^{MN} \sum_{j=1}^{MN} v_i^* v_j \text{vec}(\mathbf{X}_l)_i \text{vec}^*(\mathbf{X}_l)_j - \alpha \sum_{i=1}^{MN} \sum_{j=1}^{MN} v_i v_j^* \text{vec}^*(\mathbf{X}_l)_j \text{vec}(\mathbf{ab}^T)_i \\
&\quad - \alpha^* \sum_{i=1}^{MN} \sum_{j=1}^{MN} v_i^* v_j \text{vec}(\mathbf{X}_l)_i \text{vec}^*(\mathbf{ab}^T)_j + |\alpha|^2 \sum_{i=1}^{MN} \sum_{j=1}^{MN} v_i^* v_j \text{vec}(\mathbf{ab}^T)_i \text{vec}^*(\mathbf{ab}^T)_j. \quad (2.67)
\end{aligned}$$

The conjugate on the space-time steering vector can be switched to produce an identical result, which aids in the simplification process. Then, (2.67) can be written as

$$S = p - \alpha q^* - \alpha^* q + |\alpha|^2 r = p - 2\text{Re}(\alpha q^*) + |\alpha|^2 r, \quad (2.68)$$

where

$$p = \sum_{i=1}^{MN} \sum_{j=1}^{MN} v_i^* v_j \text{vec}(\mathbf{X}_l)_i \text{vec}^*(\mathbf{X}_l)_j, \quad (2.69)$$

$$q = \sum_{i=1}^{MN} \sum_{j=1}^{MN} v_i^* v_j \text{vec}(\mathbf{X}_l)_i \text{vec}^*(\mathbf{ab}^T)_j, \quad (2.70)$$

$$r = \sum_{i=1}^{MN} \sum_{j=1}^{MN} v_i^* v_j \text{vec}(\mathbf{ab}^T)_i \text{vec}^*(\mathbf{ab}^T)_j. \quad (2.71)$$

Equation (2.68) is quadratic with respect to α . Using the Wirtinger derivative from [28], the derivative of (2.68) can be taken with respect to α^* to find the minimum of the function:

$$\frac{dS}{d\alpha^*} = 0 - 0 - q + \alpha r \equiv 0. \quad (2.72)$$

Therefore, the solution to (2.66) and the best estimate of the LCD's complex amplitude is

$$\hat{\alpha} = \frac{q}{r}. \quad (2.73)$$

III. MATLAB Simulations

3.1 Introduction

This chapter will describe the MATLAB simulation's experimental approach and results. The MATLAB simulations are used to test the new direct solution technique from Section 2.7.1 and compare it to the original iterative method to estimating α . The MATLAB simulations are also used to assess how well the LCDR algorithm removes the LCD from the data in a controlled experiment.

3.2 Methodology

MATLAB simulations are used to generate PBR data with an LCD, estimate the LCD's spatial frequency, Doppler frequency, and complex amplitude, and remove it from the data cube. The simulation assumes the receiver is an ULA with half-wavelength spacing on an airborne platform in a side-looking configuration. There are $N = 8$ channels, $M = 32$ pulses, and $L = 49$ range bins.

Figure 3.1 shows the Cartesian coordinates in the x-y plane of the transmitter (814 m, 1410 m, 60 m), receiver (0 m, 0 m, 1000 m), and LCD (3300 m, 665 m, 0 m). With this configuration, the return from the LCD will predominantly reside in the training data.

LTE signals are used as the transmit signal and the clutter is simulated using the model described in Section 2.3.3 and [10]. The estimated interference covariance matrix is calculated through SMI from (2.46). In scenarios with no prior knowledge of the area of interest, $\hat{\mathbf{R}}_u$ must be estimated from the finite data available. The data from cells not under test are used to estimate the interference in the CUT.

Once the data cube is simulated, steps two and three are executed as outlined in Section 2.6. The amplitude is estimated using the direct solve method outlined in Section 2.7.1. The LCD is subtracted from the data using (2.63).

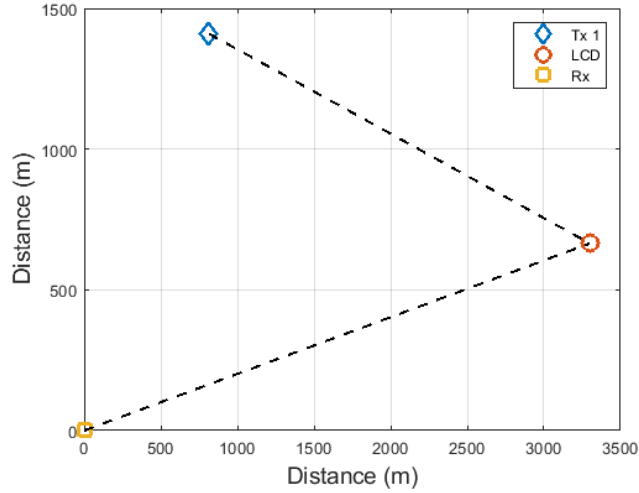


Figure 3.1: Cartesian coordinates of transmitter, LCD, and receiver in the x-y plane. The LCD resides in the training data.

3.3 Results

3.3.1 Metrics.

A common measure of performance is SINR which compares the signal's power in relation to interference and noise. The SINR obtained when using the SMI interference covariance matrix estimate is

$$SINR = \frac{\rho^2 \xi_R |\mathbf{v}^H \hat{\mathbf{R}}_u^{-1} \mathbf{v}|^2}{\mathbf{v}^H \hat{\mathbf{R}}_u^{-1} \mathbf{R}_u \hat{\mathbf{R}}_u^{-1} \mathbf{v}}, \quad (3.1)$$

where ρ^2 is the noise power and ξ_R is the single-pulse SNR for a single antenna element on receive. The optimum SNR in a noise only environment is $SNR_0 = MN\xi_R$. The purpose of adaptive filtering is to reduce clutter interference. Therefore, it is useful to analyze a STAP system's performance with interference and noise relative to the system's performance with only noise. The SINR loss, $SINR_L$, of a space-time processing algorithm is defined to be its performance relative to the matched filter SNR in an interference free environment [26].

Therefore,

$$\begin{aligned} SINR_L &= \frac{SINR}{SNR_0} \\ &= \frac{\rho^2 |\mathbf{v}^H \hat{\mathbf{R}}_u^{-1} \mathbf{v}|^2}{NM \mathbf{v}^H \hat{\mathbf{R}}_u^{-1} \mathbf{R}_u \hat{\mathbf{R}}_u^{-1} \mathbf{v}}. \end{aligned} \quad (3.2)$$

The SINR loss falls between zero and one. An SINR loss closer to one (0 dB), means the power from clutter interference is very low and the SINR is approximately equal to the SNR. Therefore, the adaptive filter is performing well by suppressing the maximum amount of clutter. Conversely, SINR loss closer to 0 (large negative number in dB) occurs when the $SNR > SINR$, which means interference from clutter is still high causing a low SINR. Thus, it is desirable to have an SINR loss closer to one (0 dB), which indicates the adaptive filter is performing well.

The PSD, a measure of the signal's power content versus frequency, is also calculated to analyze the data before and after the LCD is removed. The estimated PSD is

$$\hat{P}(\vartheta, \omega) = \frac{1}{W^2} \left| \sum_{w_1=0}^{W-1} \sum_{w_2=0}^{W-1} \mathbf{X}_l[w_1, w_2] e^{-j2\pi(w_1 \frac{\vartheta}{W} + w_2 \frac{\omega}{W})} \right|^2, \quad \vartheta, \omega \in [-0.5, 0.5], \quad (3.3)$$

which is the magnitude squared of the two-dimensional discrete Fourier transform (DFT) of the CUT, scaled by the number of samples in the DFT, W , squared.

3.3.2 Processing Time.

Results from multiple trials were recorded to analyze processing time where the LCD's $RCS = 100$. One of the motivations of this research is to improve the processing time to estimate the LCD's complex amplitude. Table 3.1 shows the average execution time and standard deviation (STD) from 200 trials for the original grid search method and the new quadratic solution outlined in Section 2.7.1. Processing time decreases by a factor of approximately 300,000 with the new quadratic method.

The grid search method originally published in [11] calls for a user defined threshold to complete the grid search method. The grid search method continues until (2.62) reaches

Table 3.1: Average and STD processing time for each method, grid search and quadratic solution, after 200 trials.

Method	Grid Search:	Quadratic Solution:
Processing time		
Avg (s)	81.09	2.46e-04
STD (s)	2.66	3.12e-04

that threshold. The threshold used for the processing time analysis is -120 dB. The quadratic solution method produces a $\hat{\alpha}$ where (2.62) evaluates to approximately -120 dB. Therefore, both methods are finding very similar $\hat{\alpha}$ with different approaches.

3.3.3 SINR Loss.

The SINR loss is calculated at $\hat{\vartheta}_{LCD} = \hat{\omega}_{LCD} = -0.05$ before and after the LCDR algorithm. The RCS of the LCD is varied to evaluate how it impacts the SINR loss. The RCS impacts the clutter-to-noise ratio (CNR) at the LCD’s spatial/Doppler frequency. As seen in Table 3.2, the larger the RCS, the larger the CNR. In this simulation, the average CNR of the homogeneous clutter is -30.31 dB. Therefore, the LCD is still “brighter” than the surrounding clutter in all three scenarios.

Table 3.2: Relating RCS to CNR

	RCS = 10	RCS = 100	RCS = 1000
CNR (dB)	-2.065	7.394	17.934

Figure 3.2 displays the SINR loss for each RCS variation before and after the LCDR algorithm. As the RCS increases, the SINR loss decreases at the clutter notch. However, after the LCDR algorithm, the SINR loss increases to a similar level, approximately -3 dB,

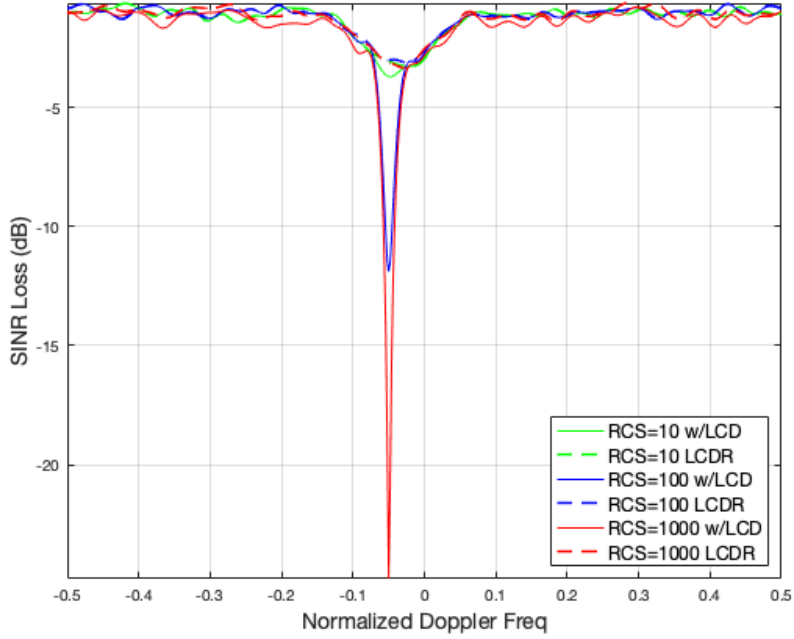


Figure 3.2: Comparison of SINR loss at $\vartheta = -0.05$ for each RCS before and after the LCDR algorithm.

for each scenario. This means the LCDR algorithm can remove LCDs of varying RCS and achieve the same results.

The SINR loss after the LCDR algorithm is used to determine if the complex amplitude estimate is accurate enough to successfully remove the LCD from the data. The goal is to improve the SINR loss at the clutter notch to approximately -3.5 dB, which is the level of SINR loss with homogeneous clutter and no LCD. Improving SINR is directly related to improving probability of detection. Table 3.3 shows the average SINR loss for 100 trials. For all RCS variations, the average SINR loss at $\hat{\vartheta}_{LCD} = \hat{\omega}_{LCD} = -0.05$ after the LCDR algorithm is greater than -3.5 dB. Therefore, (2.73) successfully estimates α .

Table 3.3 displays the SINR loss results when the LCD's amplitude is calculated through the original grid search method and the new quadratic solution method. As

mentioned in Section 3.3.2, both methods produce very similar results. Therefore, the SINR loss levels are the same for each method. However, the grid search method failed to converge to a minimum on many of the trials when the RCS = 1000.

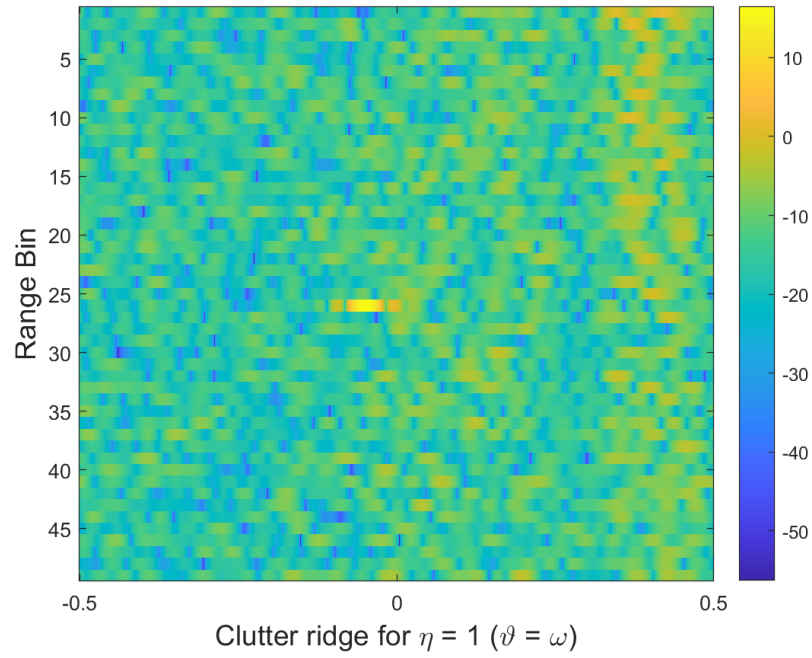
3.3.4 Power Spectral Density (PSD).

The PSD is calculated using (3.3) at the LCD's spatial/Doppler frequency $\hat{\vartheta}_{LCD} = \hat{\omega}_{LCD} = -0.05$. The PSD of the clutter ridge for each range bin over normalized frequency before and after the LCDR algorithm can be seen in Figures 3.3a and 3.3b. The PSD of an LCD with RCS = 100 can be seen in Figure 3.3a with a strong response in range bin 26. Figure 3.3b shows the PSD after the LCD is removed. The PSD at the LCD's range bin and spatial/Doppler frequency reduces from $\hat{P}(\hat{\omega}_{LCD}) = 15.93$ dB to $\hat{P}(\hat{\omega}_{LCD}) = -45.19$ dB showing that the power from the LCD is smaller.

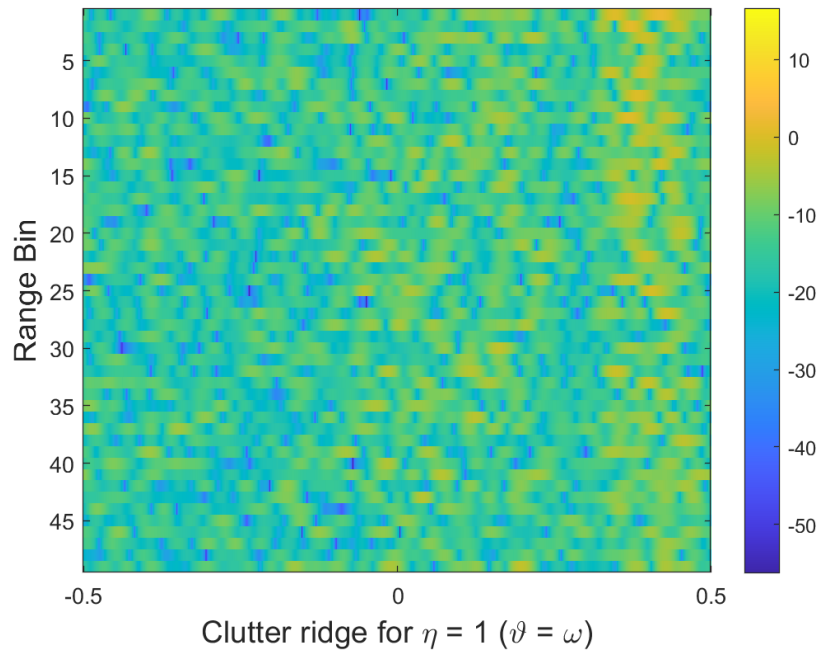
Table 3.3: Average SINR Loss and PSD after 100 trials for multiple RCS's.

Metric \ RCS	10	100	1000
SINR_L (dB)			
No LCDR	-4.48	-9.53	-17.92
LCDR Method:			
Grid Search	-3.101	-3.097	N/A
Quadratic Solution	-3.101	-3.097	-3.102
PSD (dB)			
No LCDR	0.137	16.29	26.32
LCDR Method:			
Grid Search	-50.20	-49.91	N/A
Quadratic Solution	-50.20	-49.91	-50.48

Table 3.3 lists the average PSD after 100 trials before and after the LCDR algorithm. The average PSD at the clutter ridge at all range bins is -11.42 dB. The goal is to remove the LCD so the clutter can be treated as homogeneous. Therefore, it is desirable for the PSD at the LCD's spatial/Doppler frequency to drop near or below -11.42 dB after the LCDR algorithm. As seen in Table 3.3, the PSD drops to around -50 dB for all RCS variations. This adds to the evidences in Section 3.3.3 that (2.73) accurately estimates the LCD's complex amplitude, which leads to a successful removal of the LCD.



(a) $\hat{P}(\hat{\omega}_{LCD}) = 15.93$ dB with LCD in training data.



(b) $\hat{P}(\hat{\omega}_{LCD}) = -45.19$ dB after LCDR algorithm

Figure 3.3: PSD calculated across the clutter ridge for each range bin before and after the LCDR algorithm. The LCD resides in the training data.

IV. Hardware Experiment

4.1 Introduction

This section will provide the methodology and results for the hardware experiment. This is the first time the LCDR algorithm is tested in a laboratory with hardware. The laboratory experiments are conducted to evaluate the algorithm's ability to detect and remove an LCD from experimental data.

4.2 Methodology

This section will explain the hardware experiment set up used to test the LCDR algorithm. The hardware experiment generates an LFM pulsed radar signal and transmits it from a stationary platform to a scene with a large metal cylinder acting as the LCD. The signal is received by a phased array, which is moving on a linear actuator. Figure 4.1 shows the experiment flow chart. The following sections will cover each step in the flow chart to explain the experiment.

Figure 4.2 shows the radar control graphical user interface (GUI) created in MATLAB to control the waveform generator, linear actuator, and oscilloscope. The MATLAB GUI is used to coordinate the data collection and movement of the phased array. The GUI was specifically developed for this research and was based on previous GUI versions developed by past students. The communication protocol with the waveform generator and oscilloscope needed to be updated because previous versions struggled to connect with the equipment consistently.

4.2.1 LFM Transmit Signal.

The MATLAB simulations discussed in Chapter 3 use LTE signals as the transmit waveform, as typical in passive bistatic STAP. However, the experiment must be adapted to the available hardware resources and space. The range resolution with the LTE signals



Figure 4.1: Flow chart showing steps in the hardware experiment.

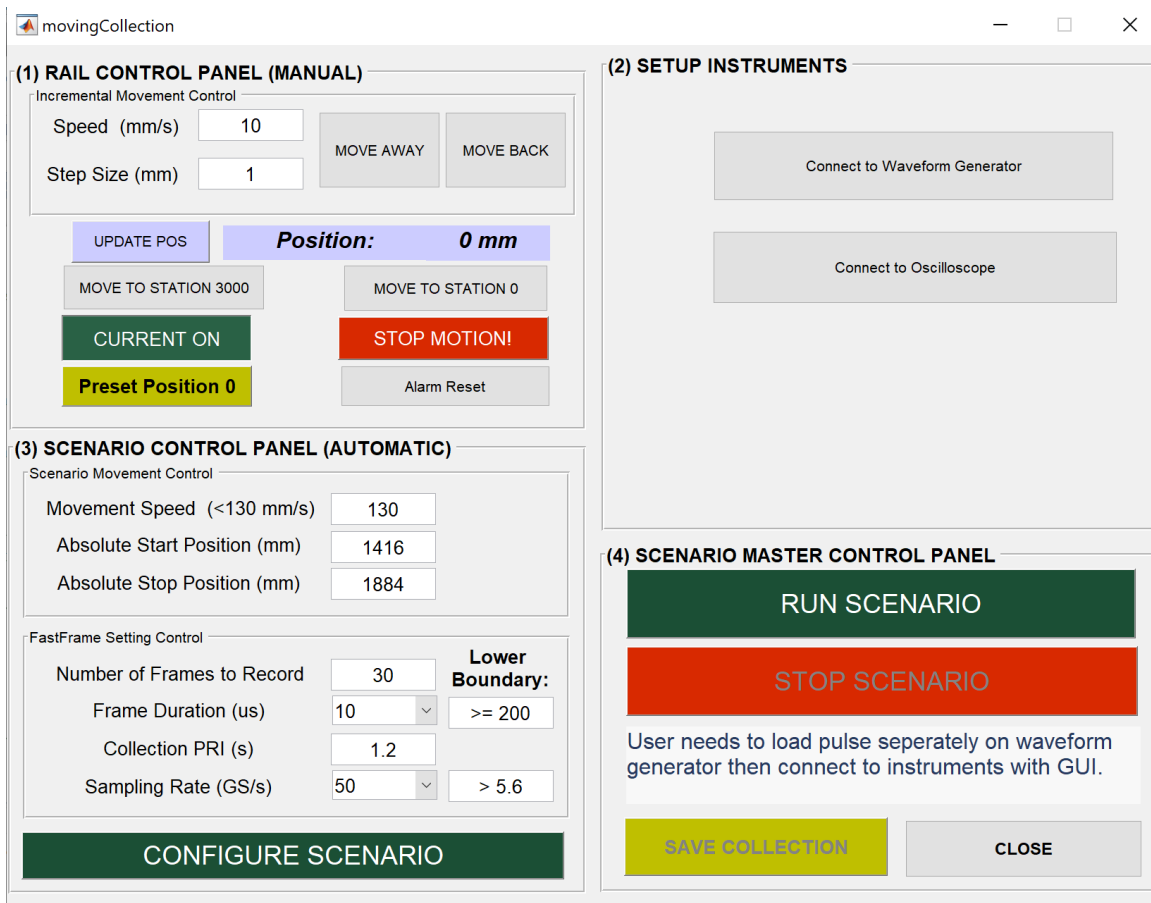


Figure 4.2: Radar control GUI created on MATLAB to command the waveform generator, linear actuator, and oscilloscope.

is 7.5 m, which is not suitable for the laboratory space. Therefore, an LFM radar pulse is used for the transmit signal in the hardware experiments. The transmit signal follows the signal model described in Section 2.2.1. The signal parameters are as follows:

- **Carrier frequency:** $f_0 = 5.2$ GHz
- **Bandwidth:** $B = 0.3$ GHz
- **Pulse width:** $\tau_c = 0.5$ μ s
- **Time-Bandwidth product:** $\tau_c B = 150$
- **PRF:** $f_r = 13$ Hz
- **Sample rate:** $f_s = 25$ GHz
- **Pulses:** $M = 30$
- **Range resolution:** $\Delta R_{LFM} = 0.5$ m
- **Clutter ridge slope:** $\eta = 1/9$

The carrier frequency and bandwidth are chosen based on the phased array specifications outline in Section 4.2.5. The PRF is chosen based on the maximum speed of the linear actuator, 130 mm/s, the desired clutter ridge slope η from (2.45), and the available memory of the computer and arbitrary waveform generator (AWG). For the AWG, the maximum sample rate is $f_s = 25$ GHz and the memory capacity is 2 Gsamples. The MATLAB simulations from Chapter 3 have a clutter ridge slope of $\eta = 1$, which results in no aliasing in the spatial or Doppler frequency domain. To achieve $\eta = 1$ with the hardware experiment, the PRF would need to be $f_r = 1.44$ Hz. However, with $f_s = 25$ GHz and a PRI of $1/f_r = 0.23$ s the number of samples is too large for the AWG's memory. Therefore, a PRF of $f_r = 13$ Hz and $\eta = 1/9$ are chosen because of the AWG memory constraints.

The pulse width is chosen to be $\tau_c = 0.5 \mu\text{s}$. Because the signal is LFM, the pulse width does not impact the range resolution. From (2.16), the range resolution depends on the bandwidth. However, the pulse width impacts the time-bandwidth product, $\tau_c B$. The number of pulses is chosen to balance resolution in the Doppler frequency domain and computer processing time.

4.2.2 Arbitrary Waveform Generator (AWG).

After the LFM pulse is created in MATLAB, the signal is manually uploaded to the Tektronix AWG (model: AWG70002A). As mentioned in Section 4.2.1, the maximum sample rate is $f_s = 25 \text{ GHz}$ and the memory capacity is 2 GSamples. One output channel is connected to the transmit antenna and the other output channel is connected to the oscilloscope to be used as a reference signal.

4.2.3 Transmit Antenna.

The transmit antenna is an airMAX Sector (model: AM-5G16-120) from Ubiquiti Networks. The antenna's frequency range is 5.10 - 5.85 GHz and it can transmit both horizontal and vertical polarized signals. As seen in Figure 4.3, the antenna patterns for both the horizontal and vertical polarization are wide in azimuth. It is advantageous for the antenna pattern to be narrow in azimuth and wide in elevation to reduce background clutter in the laboratory and have better reflection of the LCD (i.e., the metal cylinder). Therefore, the transmit antenna is rotated 90° to lie on its side, which can be seen in Figure 4.5. Additionally, for the best reflection off the LCD, the signal polarization should be vertical. The AWG is connected to the horizontal port, but the transmitted signal will actually be vertical because rotating the antenna 90° switches the polarization.

4.2.4 Area of Interest.

The area of interest the radar signal traverses can be seen in Figure 4.4 and 4.5. The distances shown are where the phased array starts and ends. The location of the transmit antenna, LCD, and phased array have been chosen so out-of-plane angle is $\phi_{OP} \geq 30^\circ$. As

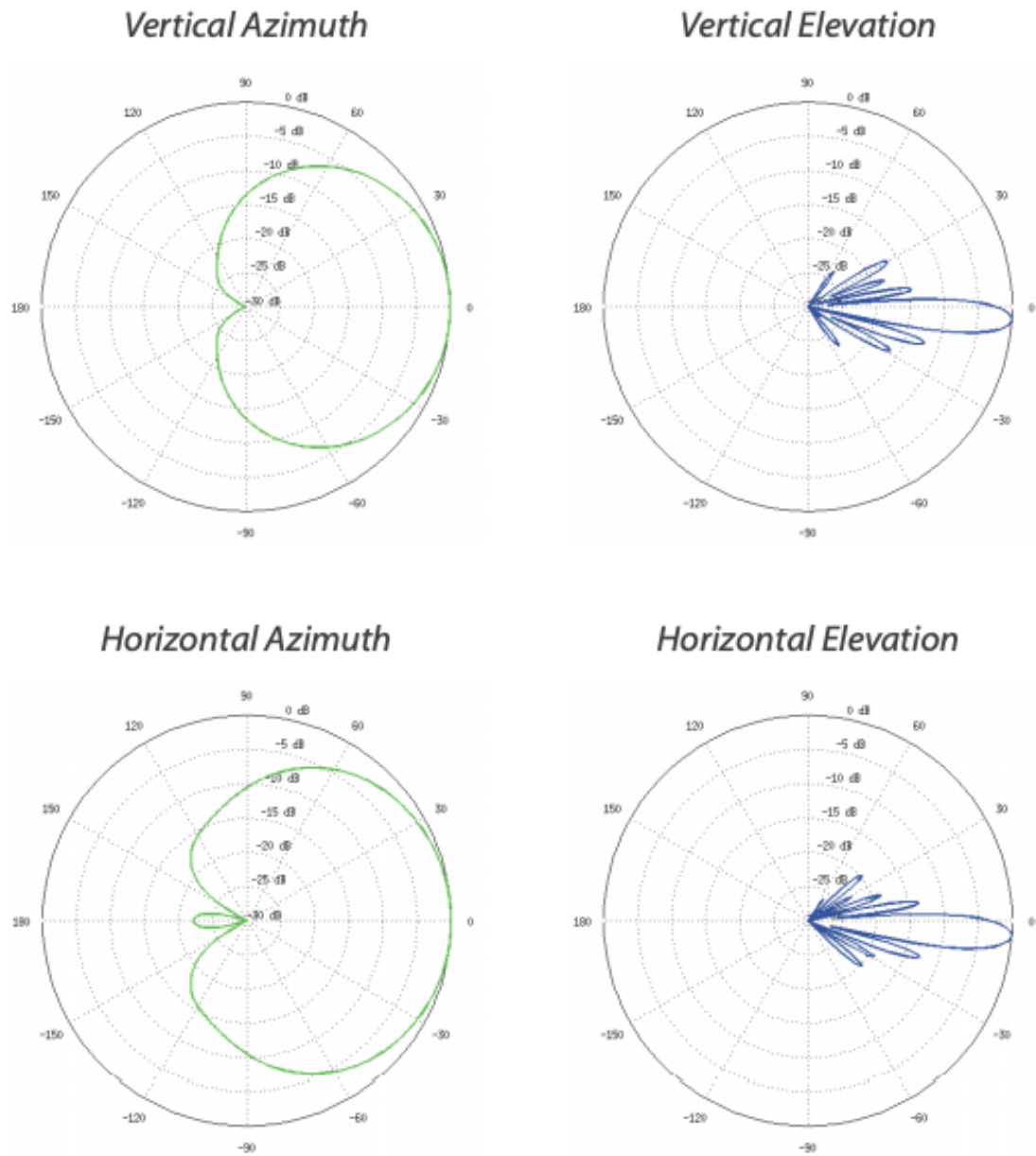


Figure 4.3: Antenna pattern for airMAX Sector (model: AM-5G16-120) from Ubiquiti Networks [25].

discovered in [11], if the out-of-plane angle is too small, the LCD can not be isolated from the rest of the clutter. In this experiment, there is very little additional clutter in the scene

because of the radar absorbing material (RAM). In a typical PBR scene, there would be homogeneous clutter in addition to an LCD. This experiment limits any additional clutter in order to focus on isolating the LCD.

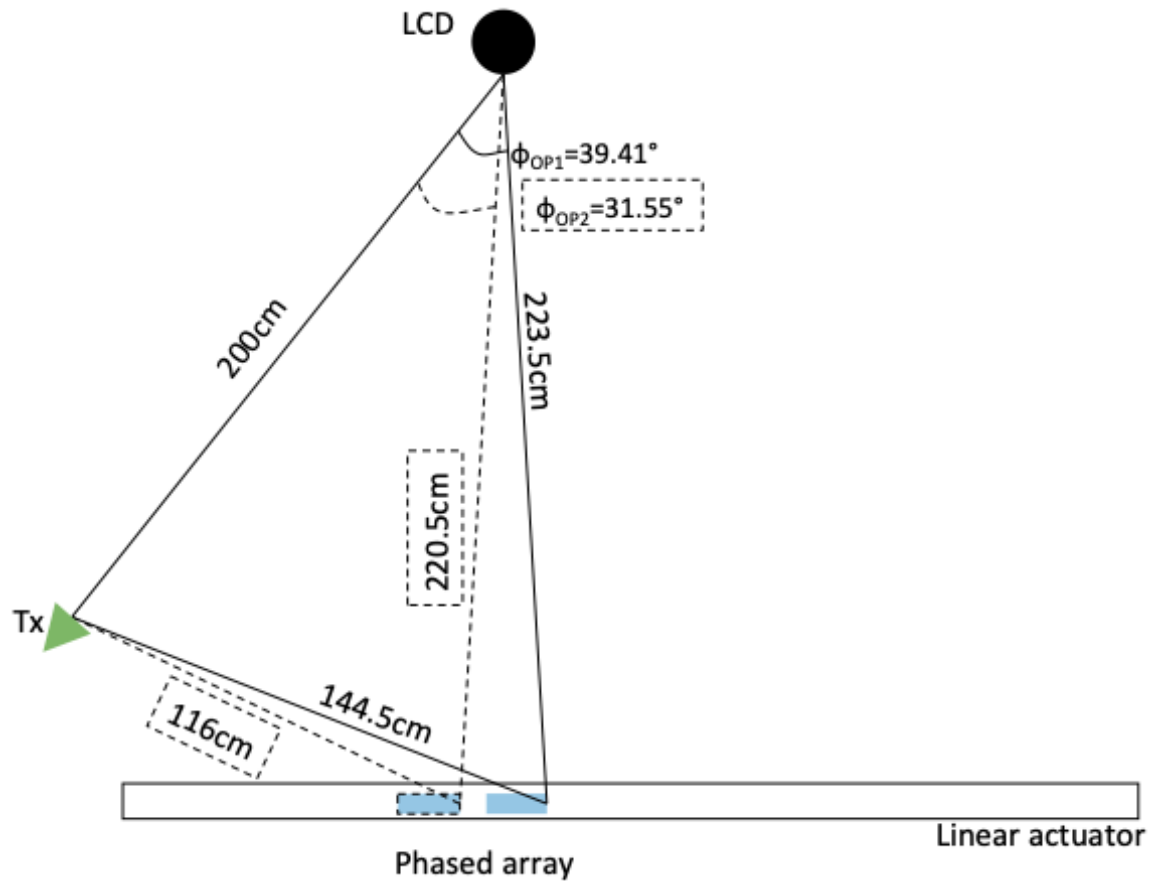


Figure 4.4: Overhead view of the hardware experiment schematic depicting the transmit antenna, LCD, and phased array on the linear actuator.

Figure 4.5 shows the hardware experiment set up in the RAIL laboratory with the transmit antenna, LCD, RAM, phased array, and linear actuator. The rotated transmit antenna causes the horizontal azimuth antenna pattern from Figure 4.3 to be wide in elevation and maximize radiation off the cylinder. The narrow azimuth radiation helps

eliminate background interference from objects in the room before the signal hits the RAM.

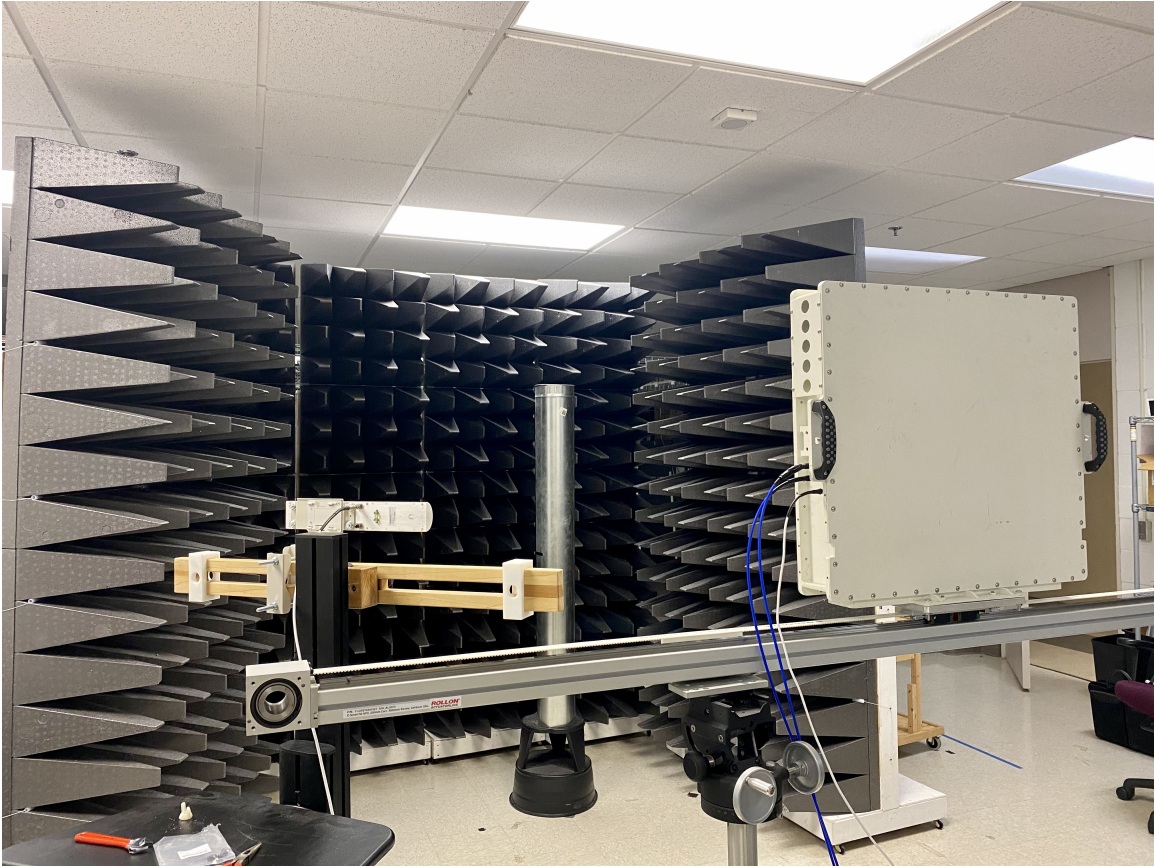


Figure 4.5: Picture of the hardware experiment set up with the transmit antenna, LCD, RAM, phased array, and linear actuator.

4.2.5 Phased Array.

A C-band phased array mounted on a linear actuator is used as the receive antenna.

The specifications are as follows:

- **Frequency:** 5.2 - 5.5 GHz
- **Lattice:** rectangular

- **Distance between channels:** $d = 9$ cm
- **Number of elements per channel:** 9×3 grid
- **Polarization:** horizontal & vertical
- **Array velocity:** $v_a = 130$ mm/s

Figure 4.6 is a diagram of the phased array showing the channels, elements, and distance between the channels. Three vertically polarized channels are used to mimic a uniform linear array. Three channels are chosen because there are only three amplifiers available. The amplifiers are high gain wideband amplifiers from Pasternack Enterprises (model number: PE15A3503) that provide approximately 44 dB gain.

Figure 4.7 shows the radiation pattern of the phase array electronically steered to 0° . Figure 4.7 is generated using the array factor equation from [18] for $-90^\circ \leq \theta \leq 90^\circ$, which is

$$AF(\theta) = \frac{1}{N} \sum_{n=1}^N \exp \left[-j \left(\frac{2\pi}{\lambda_0} nd \sin \theta \right) \right]. \quad (4.1)$$

In Figure 4.7, the main lobe is at 0° with grating lobes at $\pm 38.94^\circ$. Grating lobes are maximums that occur at angles other than the angle the phased array is electronically steered to. Grating lobes are caused by phases coherently adding at multiple angles resulting in ambiguities in direction of arrival which hinder the system's ability to locate a target. The presence of grating lobes is a consequence of the antenna design, specifically the relationship between the distance between channels and signal's wavelength. From [18], grating lobes will occur when

$$\frac{d}{\lambda_0} \sin \theta = \pm 1, \pm 2, \pm 3, \dots \quad (4.2)$$

In order to accurately measure range, Doppler frequency, and spatial frequency, the phased array needs to move at a constant velocity. The linear actuator takes about 0.6

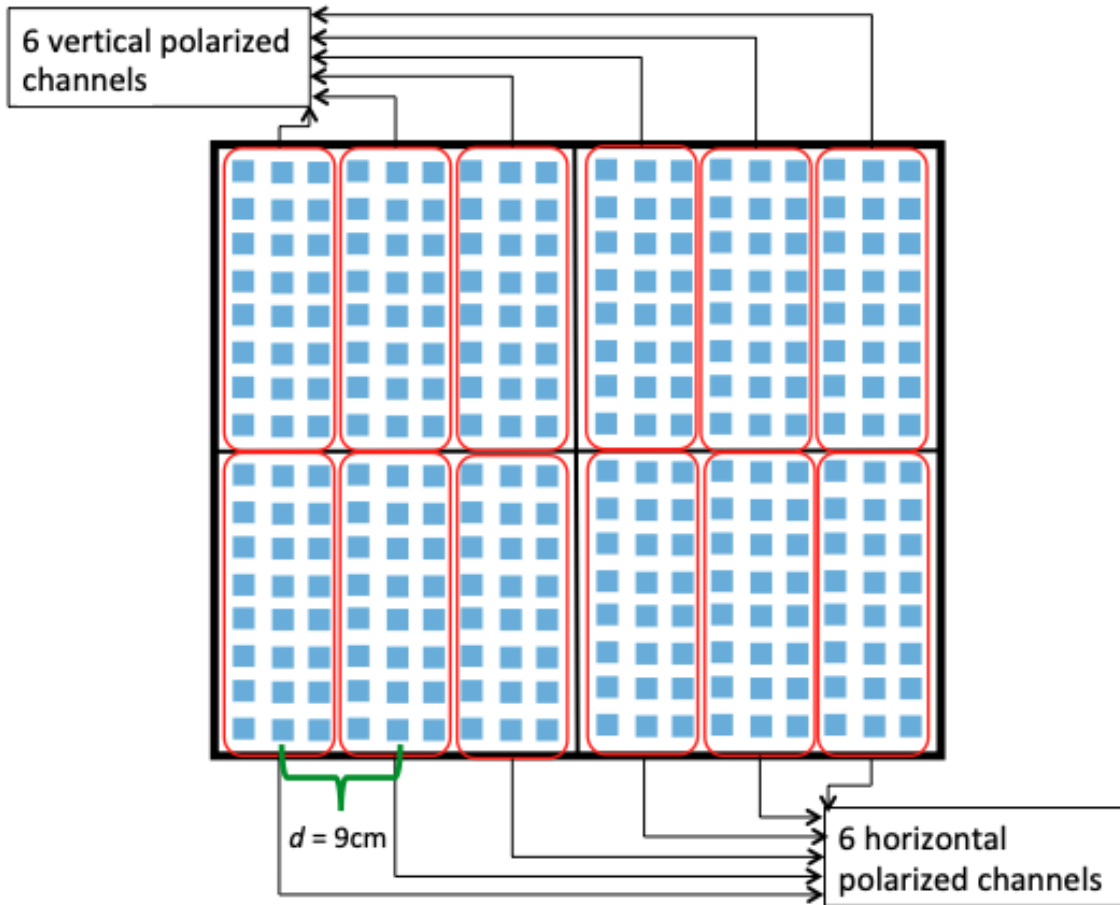


Figure 4.6: Diagram of the phased array with six horizontal and six vertical polarized channels. There are 24 elements per channel. The distance between adjacent channels is $d = 9\text{ cm}$.

s to reach constant velocity and about 0.6 s to slow down to a stop. This buffer time is added into the system so data collections happens only when the phased array is at constant velocity.

4.2.6 Oscilloscope.

After the signal passes through the amplifiers, it is sampled by a Tektronix digital phosphor oscilloscope (DPO) (model number: DPO 71254C). The AWG is connected to

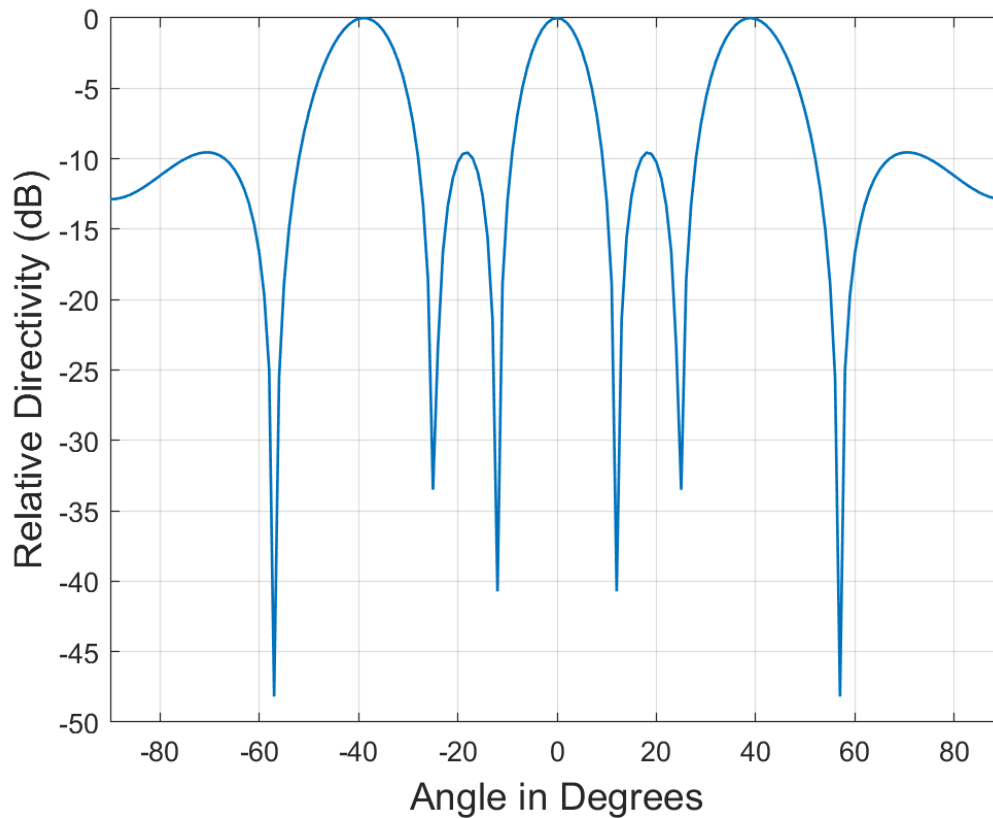


Figure 4.7: The radiation pattern of the phase array electronically steered to 0° . Grating lobes can be seen at $\pm 38.94^\circ$.

channel one and the three output channels from the phased array are connected to channels two - four. The setup can be seen in Figure 4.8. Tektronix's FastFrame Segmented Memory feature is used to sample the signal by only collecting data for a short time frame after the pulse is transmitted. The sampling frequency is 50 GHz, which is the maximum sample frequency when all four input channels are in use. The FastFrame tool is triggered by the pulse from AWG connected to channel one and samples the input channels for $10 \mu\text{s}$. This accounts for about 3000 m in total range, which is plenty of time for the pulse to travel through all the components and space to the LCD.

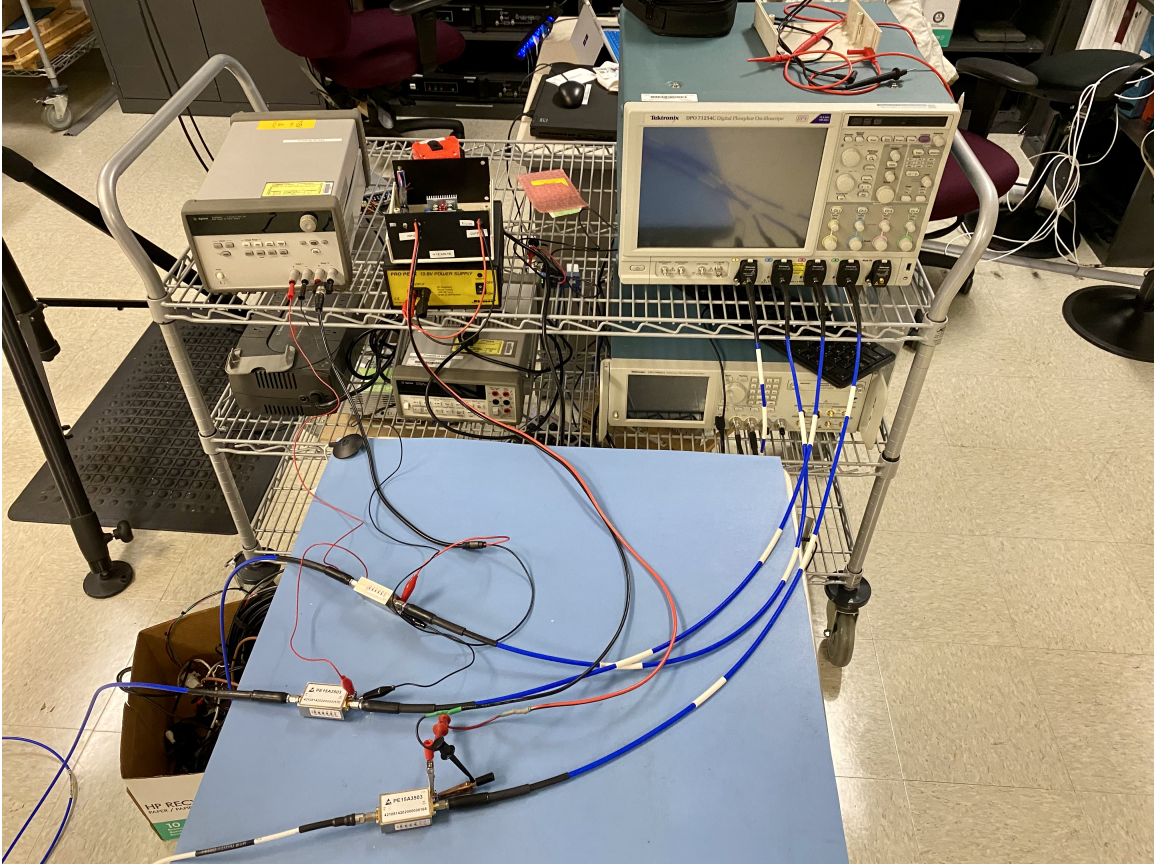


Figure 4.8: Laboratory set up with AWG on the middle shelf, high gain amplifiers on an electrostatic discharge mat, and oscilloscope on the top shelf.

The raw transmitted and received signals are shown in Figure 4.9. The pulse returned from the LCD can clearly be seen in the received signals because interference from the room and surrounding objects is reduced with the RAM. Channels one and two use the same brand of cable and length, which is why the signals look very similar. Channel three uses a different, longer cable which introduces more interference.

4.2.7 MATLAB Analysis.

The collected data is manually transferred to a computer with MATLAB for analysis. The data is down converted, separated into in-phase and quadrature channels, and matched

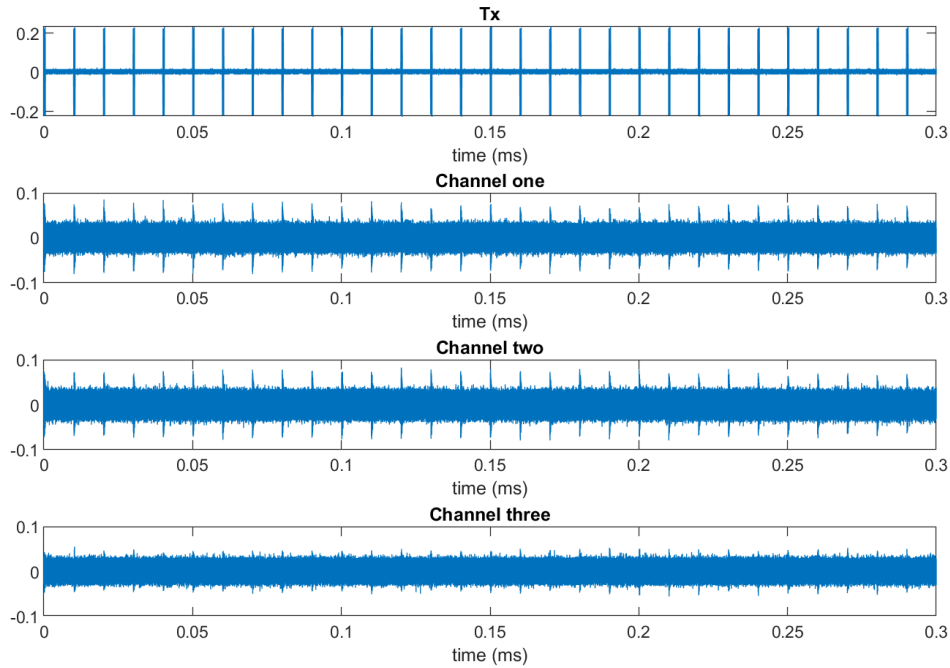


Figure 4.9: The raw transmitted and received signals from the DPO.

filtered as described in Section 2.2.1. The cables and components add delay to the pulse not associated with the range of the LCD. This delay is measured by placing the transmitter where the LCD is and capturing pulsed data on all channels. Since the range between the transmitter and the phased array is known, any additional delay is from the cables and components. This delay is constant and accounted for during the experiments.

As noted in Section 4.2.1, $\Delta R_{LFM} = 0.5$ m, which is the size of each range bin. The total range only changes by 3 cm as the phased array moves along the linear actuator, as seen in Figure 4.4. Therefore, there is no range migration, which means the peak of the matched filter is always in the same range bin for every channel and pulse. Figure 4.10 shows the matched filter response, which is calculated by taking the discrete time convolution of the received signal and the matched filter, similar to (2.14). There are 11

range bins that span from 0 m - 5.5 m. The LCD predominantly resides in range bin nine. The matched filter results are down sampled so there is one sample per range bin. The data cube can be constructed with the down sampled data.

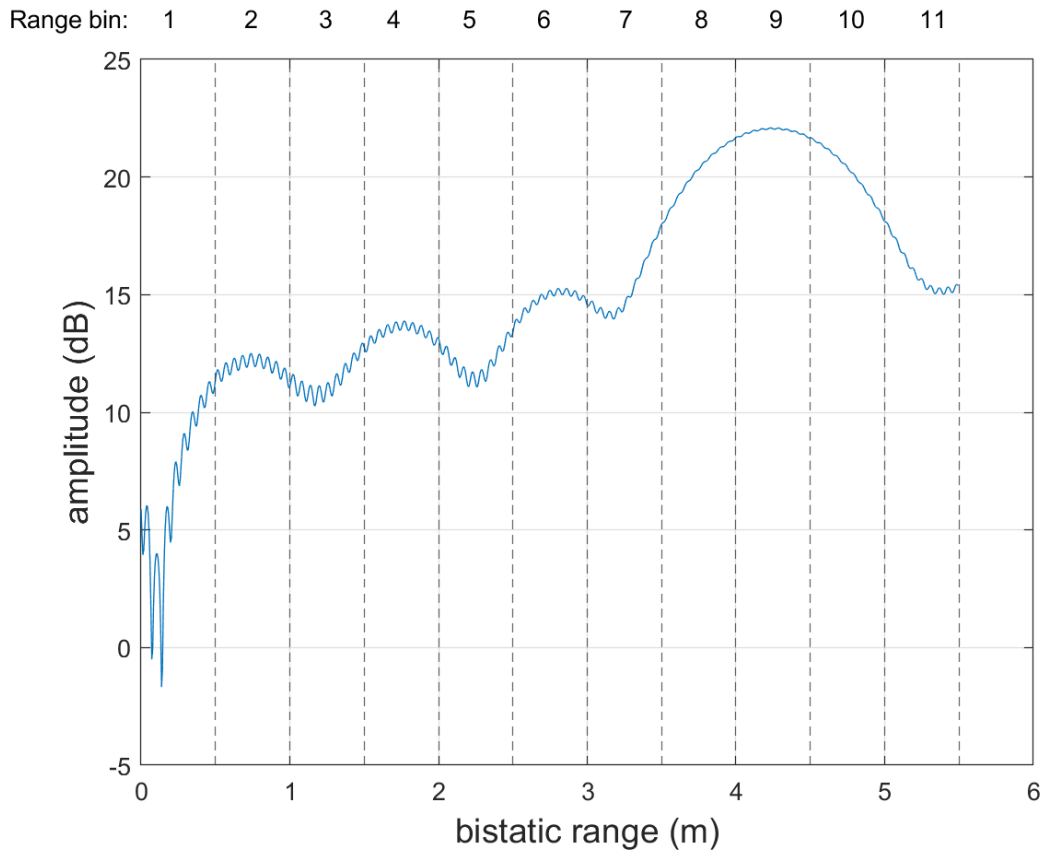


Figure 4.10: The matched filter response from channel one and pulse 10 before the data is down sampled. The dashed lines represent each range bin. The LCD predominately resides in range bin nine.

A modified LCDR algorithm is run on the data. The modifications are summarized below:

1. Determine which range bin contains the peak response from the LCD by using the true total range
2. Estimate the LCD's location in angle-Doppler
 - (a) Estimate the LCD's Doppler frequency using a one-dimensional Capon power estimator [2]
 - (b) Calculate the spatial frequency using the clutter slope, (2.45)
3. Estimate the complex amplitude of the LCD using the method from Section 2.7.1
4. Subtract the LCD from the data cube using normalized scale factors to account for energy spread across adjacent range bins, (4.4)

The laboratory environment did not allow for appropriate experimentation of step one. With the use of RAM, there is no other clutter the detector needs to distinguish the LCD from. Additionally, the out-of-plane angle would likely have little impact on the detection. Therefore, this proof of concept focused on steps two through four. For step two, a one-dimensional Capon estimator is used to estimate the Doppler frequency. The data has finer resolution in the Doppler domain than the spatial domain because there are only three channels. The sub-sequence length from Section 2.6.2 is $L_M = 15$ because using more pulses produced inconsistent Doppler frequency estimations. Then, (2.45) is used to calculate the spatial frequency. The LCD's complex amplitude is calculated as described in Section 2.7.1.

The LCDR algorithm uses (2.63) to subtract the LCD from the data cube. As seen in Figure 4.10, the peak of the matched filter is centered in range bin nine, but the main lobe and side lobes extend to adjacent range bins. Equation (2.63), as published in [11], uses the auto-correlation of the transmit signal to account for how the matched filter spreads across range bins. However, using the theoretical auto-correlation from (2.15)

or the auto-correlation from channel one of the DPO with the hardware data does not sufficiently reduce the energy spread across range bins. The auto-correlation function is not representative of the received signal after it has been through multiple hardware components and has had noise/interference added. The received signal from each pulse and channel will be unique. Therefore, the side lobes can be accounted for by generating a normalized data cube to act as scale factors. The data for one channel and one pulse is defined as $\mathbf{x}_{n,m}$, a $(L \times 1)$ vector. The data for each channel and pulse is normalized by

$$\mathbf{x}_{n,m}^{norm} = \frac{\mathbf{x}_{n,m}}{\arg\max_l \mathbf{x}_{n,m}}. \quad (4.3)$$

A normalized data cube, \mathbf{X}^{norm} , can be constructed by calculated (4.3) for each pulse and channel. The new data cube is constructed by subtracting the LCD from each range bin,

$$\mathbf{X}'_l = \mathbf{X}_l - \hat{\alpha} \left(\mathbf{a}(\hat{\vartheta}_{LCD}, \hat{\omega}_{LCD}) \mathbf{b}(\hat{\vartheta}_{LCD}, \hat{\omega}_{LCD})^T \right) \odot \mathbf{X}_l^{norm}. \quad (4.4)$$

4.3 Results

4.3.1 Metrics.

This hardware experiment focuses on the LCDR algorithm's ability to remove the LCD. Processing time is not examined because it was already determined in Section 3.3 that directly solving for the complex amplitude is faster than the iterative approach. The hardware experiment will not use SINR loss to analyze the results because the true interference covariance matrix is not known. The PSD, from (3.3), will be used to analyze the results before and after the LCD is removed.

4.3.2 Power Spectral Density (PSD).

The PSD is calculated for all spatial and Doppler frequencies at the range bin with the LCD, range bin nine. The LCD's spatial and Doppler frequencies is estimated using step two of the modified LCDR algorithm and are $\hat{\vartheta}_{LCD} = -0.002$ and $\hat{\omega}_{LCD} = -9.8e - 04$. The PSD of range bin nine can be seen in Figure 4.11a. The resolution is coarse over the spatial frequency because there are only three channels. Figure 4.12a shows the PSD of

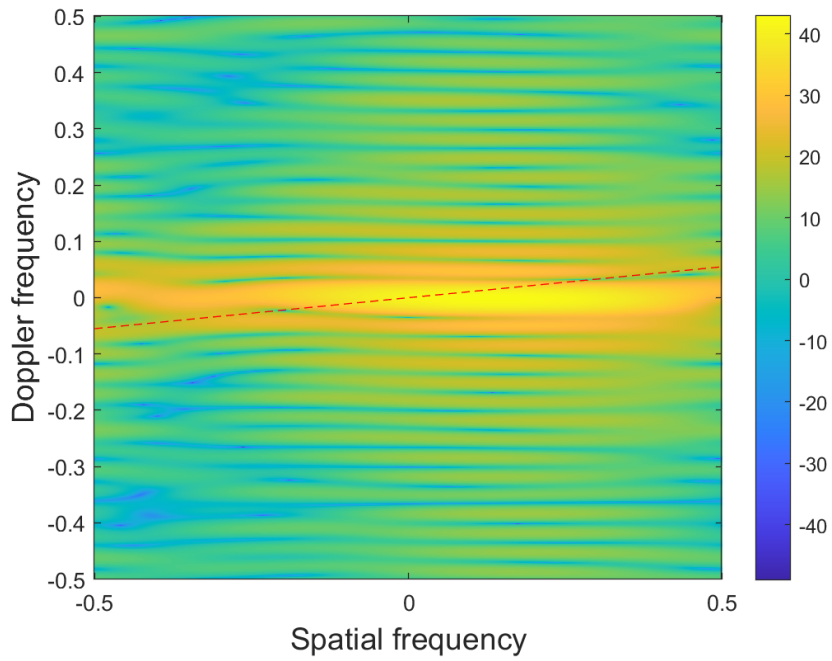
each clutter ridge across all range bins and highlights how the energy from the LCD is spread across range bins. Figure 4.12a also shows energy near $\vartheta = \pm 0.2$ which is attributed to the grating lobes peaks illustrated in Figure 4.7.

Step four from the modified LCDR algorithm discussed in Section 4.2.7 is used to remove the LCD. In Figure 4.11b the PSD of range bin nine is generated after the LCDR algorithm. The PSD at $(\hat{\vartheta}_{LCD}, \hat{\omega}_{LCD})$ drops from 41.12 dB to -48.44 dB. The average PSD of a radar collection with no LCD in the area of interest is -4.18 dB, which represents the average PSD of homogeneous clutter in the scene. The goal is remove the LCD from the data so the clutter can be treated as homogeneous and suppressed through SMI. Reducing the PSD to -48.44 dB at $(\hat{\vartheta}_{LCD}, \hat{\omega}_{LCD})$ achieves this goal because it is less than or equal to -4.18 dB. However, there is still high energy spread across all spatial frequencies around zero Doppler frequency. The algorithm is removing energy at the specific space-time location of the LCD and it does not account for the spread of energy due to the small number of channels or grating lobes. Figure 4.12b is the PSD of the clutter ridge at each range bin. The algorithm is successful at removing the energy at $\hat{\vartheta}_{LCD}$ from main lobe and adjacent side lobes. Therefore, if the LCD could be more localized with additional channels and void of grating lobes, then the LCDR algorithm may prove to be successful.

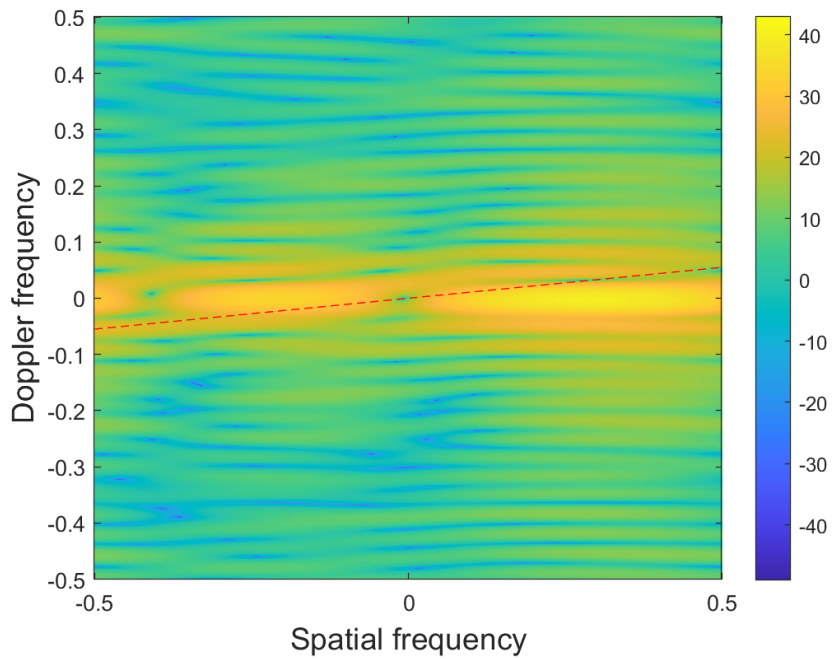
4.3.3 Matched Filter Response.

Figure 4.13 is the down sampled matched filter response for channel one and pulse 10 before and after the LCDR algorithm. The matched filter response is calculated by taking the discrete time convolution of the received signal and the matched filter, similar to (2.14), and down sampling the data so there is one sample per range bin. Figure 4.13 shows the LCDR algorithm reduces the amplitude of the matched filter response at the main and side lobes by about 2 dB and is another perspective that shows the LCDR algorithm is removing energy from the LCD across range bins. The 2 dB reduction in the matched filter equates to the approximately 88 dB drop in PSD from Figure 4.12a to Figure 4.12b. Figure 4.13

adds to the evidence that the LCDR algorithm is correctly accounting for the spread across range bins and, if the LCD could be more localized in space-time, the LCDR algorithm may prove to be successful.

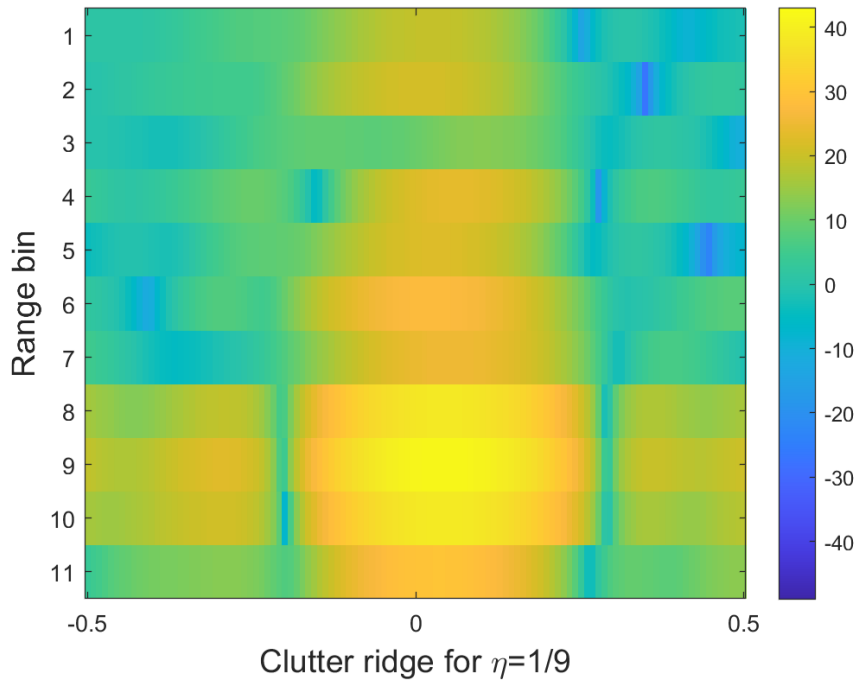


(a) Before the LCDR algorithm. $\hat{P}(\hat{\vartheta}_{LCD}, \hat{\omega}_{LCD}) = 41.12\text{dB}$.

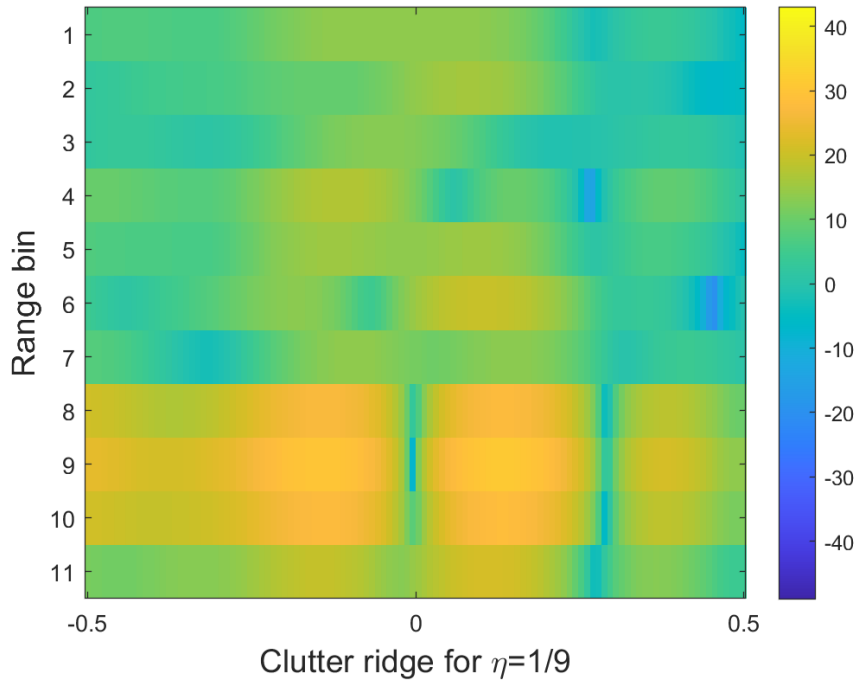


(b) After the LCDR algorithm. $\hat{P}(\vartheta_{LCD}, \omega_{LCD}) = -48.44\text{ dB}$.

Figure 4.11: PSD calculated for range bin nine over all spatial and Doppler frequencies before and after the LCDR algorithm. The red line marks the clutter ridge with slope $\eta = 1/9$.



(a) Before the LCDR algorithm. $\hat{P}(\hat{\vartheta}_{LCD}, \hat{\omega}_{LCD}) = 41.12\text{dB}$.



(b) After the LCDR algorithm. $\hat{P}(\vartheta_{LCD}, \omega_{LCD}) = -48.44\text{ dB}$.

Figure 4.12: PSD across the clutter ridge for each range bin before and after the LCDR algorithm.

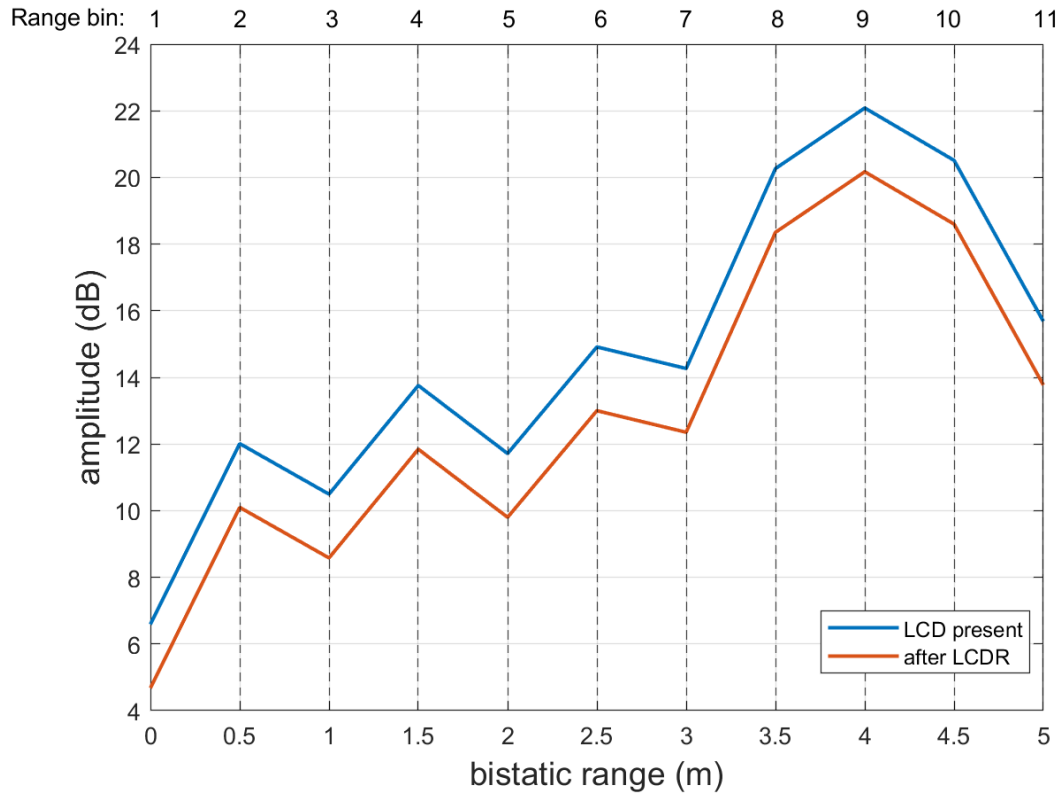


Figure 4.13: The down sampled matched filter response for channel one and pulse 10, which is the data that makes up the data cube, before and after the LCDR algorithm.

V. Conclusions and Recommendations

5.1 Introduction

The section will discuss conclusions from this research. It will review the method to solve the complex amplitude and what was gained from the MATLAB simulations and hardware experiments. Additionally, this section will provide recommendations for future research.

5.2 Conclusions

From the MATLAB simulations, it can be concluded that (2.73) accurately estimates the LCD's complex amplitude, which leads to a successful removal of the LCD. When the estimated amplitude from (2.73) is used to remove the LCD from the data, the SINR loss at the clutter notch is comparable to the SINR loss for homogeneous clutter. The goal of the LCDR algorithm is to remove the LCD from the data so the clutter can be treated as homogeneous. Additionally, the PSD at the LCD's spatial/Doppler frequency is below the average PSD of the clutter ridge at all range bins. Finally, the MATLAB simulations proved directly solving for the amplitude that minimizes the output power is faster and less complex than the previous method originally published in [11].

From the hardware experiments, it can be concluded that the LCDR algorithm can estimate the LCD's direction of arrival and complex amplitude in a laboratory environment. Additionally, the energy spread from the main lobe and side lobes can be accounted for and removed with the LCDR algorithm. However, the experiments showed there are limitations with the algorithm. The LCD was not well defined in spatial frequency because of the limited phased array channels available and grating lobes. The algorithm does not account for these issues. Therefore, the LCDR algorithm did not successfully remove all energy associated from the LCD.

Overall, this research concludes the LCDR algorithm is a promising solution to remove an LCD from STAP data. Further hardware testing is needed to determine if the algorithm can be used in real world environments.

5.3 Recommendations

This research focused on the method to estimate the complex amplitude and how that impacted the removal of the LCD. An area that could use additional research is the accuracy of the Capon estimator in step two of the LCDR algorithm. For example, the sub-sequence length can be analyzed. Additionally, the user must choose which data to perform the Capon estimator on. This research only used one channel, but it may be better to average the Capon estimate from multiple channels. Also, one could also analyze the difference between using a two-dimensional Capon estimator to solve for both the spatial and Doppler frequency and a one-dimensional Capon estimator to solve for one frequency in conjunction with the clutter ridge relationship to solve for the other frequency.

Because of the issues found during the hardware experiment, the MATLAB simulations should be expanded to model the hardware limitations and characterize the impacts on the LCDR algorithm. For example, different clutter ridge slopes, grating lobes from the phased array, or limited channels could be modeled. Additionally, mutual coupling is the electromagnetic interaction between channels on an array that can impact the radiation pattern of the array [4]. Mutual coupling is another consequence of using real hardware which could be modeled to analyze the impacts on the LCDR algorithm.

There are many options for expanding the hardware experiments. First, the experiment could be conducted with pulse diverse waveforms, as typical in PBR systems. Another improvement would be to use more channels so the data has finer resolution in the spatial frequency domain. This would also be beneficial to two-dimensional versus one-dimensional Capon estimation. Additionally, a phased array with no grating should be tested to see the impact on the results. Another factor that could be added to the hardware

experiment is a moving target. The ability of the LCDR algorithm to distinguish between a target and the LCD could be tested and analyzed.

Bibliography

- [1] Abdullah, Raja Syamsul Azmir Raja, Asem Ahmad Salah, and Nur Emileen Abdul Rashid. “Moving Target Detection by Using New LTE-Based Passive Radar”. *Progress In Electromagnetics Research B*, 63:145–160, 2015. ISSN 1937-6472. URL <http://www.jpier.org/PIERB/pier.php?paper=15070901>.
- [2] Capon, J. “High-Resolution Frequency-Wavenumber Spectrum Analysis”. *Proceedings of the IEEE*, 57:1408–1418, 1969. ISSN 15582256.
- [3] Evers, Aaron and Julie Ann Jackson. “Analysis of an LTE waveform for radar applications”. 200–205. Institute of Electrical and Electronics Engineers Inc., 2014. ISBN 9781479920341. ISSN 10975659.
- [4] Guerci, J. R. *Space-Time Adaptive Processing for Radar*. Artech House, 2015. ISBN 78-1-60807-820-2.
- [5] Harms, H. Andrew, Linda M. Davis, and James Palmer. “Understanding the signal structure in DVB-T signals for passive radar detection”. 532–537. Institute of Electrical and Electronics Engineers Inc., 2010. ISBN 9781424458127. ISSN 10975659.
- [6] Jakobsson, Andreas and Petre Stoica. “Combining Capon and APES for estimation of spectral lines”. *Circuits, Systems, and Signal Processing*, 19:159–169, 2000. ISSN 0278081X.
- [7] Li, H., J. Li, and P. Stoica. “Performance analysis of forward-backward matched-filterbank spectral estimators”. *IEEE Transactions on Signal Processing*, 46(7):1954–1966, 1998.
- [8] Li, Jian and Petre Stoica. “An adaptive filtering approach to spectral estimation and SAR imaging”. *IEEE Transactions on Signal Processing*, 44:1469–1484, 1996. ISSN 1053587X.
- [9] Lievsay, James R. “Passive Radar Clutter Modeling and Emitter Selection for Ground Moving Target Indication”, 2017.
- [10] Lievsay, James R. and Nathan A. Goodman. “Modeling Three-Dimensional Passive STAP with Heterogeneous Clutter and Pulse Diversity Waveform Effects”. *IEEE Transactions on Aerospace and Electronic Systems*, 54:861–872, 2018. ISSN 00189251.
- [11] Lievsay, James R. and Nathan A. Goodman. “Passive radar large clutter discrete removal”. *2018 IEEE Radar Conference, RadarConf 2018*, 1167–1172, 2018.

- [12] Neyt, Xavier, Jacques Raout, Mireille Kubica, Virginie Kubica, Serge Roques, Marc Acheroy, and Jacques G. Verly. “Feasibility of STAP for passive GSM-based radar”. 546–551. 2006. ISBN 0780394968. ISSN 10975659.
- [13] Page, Douglas and Gregory Owirkaa. “Knowledge-aided STAP processing for ground moving target indication radar using multilook data”. *Eurasip Journal on Applied Signal Processing*, 2006:1–16, 2006. ISSN 11108657.
- [14] Palmer, James E., H. Andrew Harms, Stephen J. Searle, and Linda M. Davis. “DVB-T passive radar signal processing”. *IEEE Transactions on Signal Processing*, 61:2116–2126, 2013. ISSN 1053587X.
- [15] Petri, Dario, Christian Moscardini, Michele Conti, Amerigo Capria, James E. Palmer, and Stephen J. Searle. “The effects of DVB-T SFN data on passive radar signal processing”. 280–285. 2013. ISBN 9781467351775.
- [16] Raout, J., X. Neyt, and P. Rischette. “Bistatic stap using DVB-T illuminators of opportunity”. 2007. ISBN 9780863418488.
- [17] Richards, M, James A Scheer, and William A Holm. *Principles of Modern Radar: Advanced Techniques*. 2008. ISBN 978-1-891121-54-8.
- [18] Richards, Mark, James Scheer, and William Holm. *Principles of Modern Radar: Basic Principles*. Scitech Publishing, inc., 2010.
- [19] Salah, Asem A., R. S.A.Raja Abdullah, A. Ismail, F. Hashim, C. Y. Leow, M. B. Roslee, and N. E.Abdul Rashid. “Feasibility study of LTE signal as a new illuminators of opportunity for passive radar applications”. 258–262. IEEE Computer Society, 2013.
- [20] Scholnik, Dan P. “Range-ambiguous clutter suppression with pulse-diverse waveforms”. 336–341. 2011. ISBN 9781424489022. ISSN 10975659.
- [21] Searle, Stephen, Stephen Howard, and James Palmer. “Remodulation of DVB-T signals for use in passive bistatic radar”. 1112–1116. 2010. ISBN 9781424497218. ISSN 10586393.
- [22] Searle, Stephen, James Palmer, and Linda Davis. “On the effects of clock offset in OFDM-based Passive Bistatic Radar”. 3846–3850. 10 2013. ISBN 9781479903566. ISSN 15206149.
- [23] Searle, Stephen, James Palmer, Linda Davis, Daniel W. O’Hagan, and Martin Ummenhofer. “Evaluation of the ambiguity function for passive radar with OFDM transmissions”. 1040–1045. Institute of Electrical and Electronics Engineers Inc., 2014. ISBN 9781479920341. ISSN 10975659.
- [24] Stoica, Petre, Hongbin Li, Jian Li, and Senior Member. “A New Derivation of the APES Filter”, 1999.

- [25] Ubiquiti Networks. *airMAX Sector Datasheet*, 2013-2018.
- [26] Ward, J. *Space-Time Adaptive Processing for Airborne Radar*. Technical Report 1015, Lincoln Laboratory MIT, Lexington, MA, USA, 1994.
- [27] Willis, Nicholas and Hugh Griffiths. *Advances in Bistatic Radar*. Scitech Publishing, 2007.
- [28] Wirtinger, W. “Zur formalen Theorie der Funktionen von mehr komplexen Veränderlichen (on the formal theory of the functions of more complex variables)”. *Mathematische Annalen (Mathematical Annals)*, 97:357–376, 1927. URL <http://eudml.org/doc/182642>.

REPORT DOCUMENTATION PAGE

Form Approved
OMB No. 0704-0188

The public reporting burden for this collection of information is estimated to average 1 hour per response, including the time for reviewing instructions, searching existing data sources, gathering and maintaining the data needed, and completing and reviewing the collection of information. Send comments regarding this burden estimate or any other aspect of this collection of information, including suggestions for reducing this burden to Department of Defense, Washington Headquarters Services, Directorate for Information Operations and Reports (0704-0188), 1215 Jefferson Davis Highway, Suite 1204, Arlington, VA 22202-4302. Respondents should be aware that notwithstanding any other provision of law, no person shall be subject to any penalty for failing to comply with a collection of information if it does not display a currently valid OMB control number. **PLEASE DO NOT RETURN YOUR FORM TO THE ABOVE ADDRESS.**

1. REPORT DATE (DD-MM-YYYY) 25-03-2021		2. REPORT TYPE Master's Thesis		3. DATES COVERED (From — To) Oct 2019–Mar 2021	
4. TITLE AND SUBTITLE Amplitude Estimation for the Large Clutter Discrete Removal Algorithm				5a. CONTRACT NUMBER	
				5b. GRANT NUMBER	
				5c. PROGRAM ELEMENT NUMBER	
				5d. PROJECT NUMBER	
				5e. TASK NUMBER	
				5f. WORK UNIT NUMBER	
6. AUTHOR(S) Gjeremo Chomitz, Hanna, 1st Lt, USAF				8. PERFORMING ORGANIZATION REPORT NUMBER AFIT-MS-ENG-21-M-40	
				11. SPONSOR/MONITOR'S REPORT NUMBER(S)	
9. SPONSORING / MONITORING AGENCY NAME(S) AND ADDRESS(ES) Intentionally left blank				8. PERFORMING ORGANIZATION NAME(S) AND ADDRESS(ES) Air Force Institute of Technology Graduate School of Engineering and Management (AFIT/EN) 2950 Hobson Way WPAFB, OH 45433-7765	
				10. SPONSOR/MONITOR'S ACRONYM(S)	
12. DISTRIBUTION / AVAILABILITY STATEMENT DISTRIBUTION STATEMENT A: APPROVED FOR PUBLIC RELEASE; DISTRIBUTION UNLIMITED					
13. SUPPLEMENTARY NOTES This work is declared a work of the U.S. Government and is not subject to copyright protection in the United States.					
14. ABSTRACT A large clutter discrete (LCD) is spectrally bright localized clutter that can cause a false alarm or missed target detection in space-time adaptive processing (STAP) radar data. For passive bistatic STAP, the four step LCD removal (LCDR) algorithm estimates the spatial/Doppler frequency and complex amplitude of the LCD and then removes it from the data. Once the LCD is removed from the data, homogeneous clutter suppression techniques can be used to process the data and search for targets. This research focuses on reducing the complexity of estimating the LCD's complex amplitude. This research proposes a method that directly solves for the amplitude that minimizes the power output at the LCD's spatial/Doppler frequency. This research also focuses on further verifying the LCDR algorithm through hardware experimentation. Previously, the algorithm has only been tested through simulation. First, the amplitude estimation technique is tested through MATLAB simulations to determine the efficiency and accuracy of the proposed method. Then, a hardware experiment is used to test the amplitude estimation technique and verify the LCDR algorithm in a laboratory environment. The MATLAB simulations prove the proposed amplitude estimation technique is faster than the original method published in [11]. The LCDR algorithm is able to successfully remove the LCD in the simulated data so the clutter can be treated as homogeneous. The hardware results are less conclusive. The hardware adds additional complications to the data because of grating lobes and the limited number of channels available. However, the LCDR algorithm is able to remove portions of the LCD and shows promise of being successful in more real world environments.					
15. SUBJECT TERMS Radar, STAP, signal processing, clutter					
16. SECURITY CLASSIFICATION OF:			17. LIMITATION OF ABSTRACT	18. NUMBER OF PAGES	19a. NAME OF RESPONSIBLE PERSON (ENG)
a. REPORT	b. ABSTRACT	c. THIS PAGE			19b. TELEPHONE NUMBER (include area code)
U	U	U	UU	82	(937) 255-3636 ext. 7469